AMERICAN UNIVERSITY OF BEIRUT

High Sensitivity Inkjet-printed Organic Electrochemical Transistors (OECTs) for Applications in Heart Disease Point-of-Care Diagnostics

by
Mhd Walid Mhd Ayman AlChamaa

A thesis
submitted in partial fulfillment of the requirements
for the degree of Master of Science
to the Program of Biomedical Engineering
of the Maroun Semaan Faculty of Engineering and Architecture
at the American University of Beirut

Beirut, Lebanon
December 2020

AMERICAN UNIVERSITY OF BEIRUT

High Sensitivity Inkjet-printed Organic Electrochemical Transistors (OECTs) for Applications in Heart Disease Point-of-Care Diagnostics

by
Mhd Walid Mhd Ayman AlChamaa

Approved by:

_____

Prof. Massoud Khraiche, Assistant Professor   Advisor

Biomedical Engineering

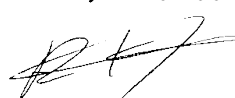_____

Prof. Samir Alam, Professor   Co-advisor

Internal Medicine

_____

Prof. Zaher Dawy, Professor   Member of Committee

Electrical and Computer Engineering

_____

Prof. Rouwaida Kanj, Associate Professor   Member of Committee

Electrical and Computer Engineering

Date of thesis defense: December 14, 2020

AMERICAN UNIVERSITY OF BEIRUT

THESIS, DISSERTATION, PROJECT RELEASE FORM

Student Name: __AlChamaa_____Mhd Walid_____Mhd Ayman__
                                Last   First   Middle

☑ Master's Thesis   ◯ Master's Project   ◯ Doctoral Dissertation

☐   I authorize the American University of Beirut to: (a) reproduce hard or electronic copies of my thesis, dissertation, or project; (b) include such copies in the archives and digital repositories of the University; and (c) make freely available such copies to third parties for research or educational purposes.

☑   I authorize the American University of Beirut, to: (a) reproduce hard or electronic copies of it; (b) include such copies in the archives and digital repositories of the University; and (c) make freely available such copies to third parties for research or educational purposes after:

      One ___ **year from the date of submission of my thesis, dissertation or project.**
      Two ___ **years from the date of submission of my thesis , dissertation or project.**
      Three __ **years from the date of submission of my thesis , dissertation or project.**

_____   02/06/2021
        Signature   Date

This form is signed when submitting the thesis, dissertation, or project to the University Libraries

Acknowledgements

Firstly, I would like to thank everyone who had contributed to the successful completion of this thesis. My recognition and gratitude are addressed to my advisor, Prof. Massoud Khraiche for his continuous guidance and support. I would like to thank all my committee members for the insightful comments and helpful feedback. Special thanks to Prof. Zaher Dawy for his continuous guidance and support.

I would like to express my gratitude to my loving parents and friends who had helped and given me encouragement. Special thanks to my lab colleagues, especially Reem Almasri, Rima El-Hassan, Zeina Habli, and Sahera Saleh for the exciting and thought-provoking scientific discussions that we engaged in and the wonderful company over the past couple of years. I would also like to thank Mr. Ali Kanso for his priceless help in the software development.

An Abstract of the Thesis of

Mhd Walid Mhd Ayman AlChamaa   for   Master of Science
                                                       Major: Biomedical Engineering

Title: High Sensitivity Inkjet-printed Organic Electrochemical Transistors (OECTs) for Applications in Heart Disease Point-of-Care Diagnostics

Heart failure, a class of cardiovascular diseases, is one of the leading causes of death worldwide. Early detection of heart disease has a major impact on slowing down disease progression and improving patient outcomes. B-type natriuretic peptide (BNP) and its N-terminal prohormone (NT-proBNP) are HF biomarkers that have high diagnostic and prognostic value. In this work, we developed a point-of-care biosensing platform for the detection of B-type natriuretic peptide (BNP) and its N-terminal prohormone (NT-proBNP) via organic electrochemical transistors (OECTs). The OECTs were built using state-of-the-art inkjet printing technology, a scalable, highly reproducible, and low-cost fabrication process. The inkjet technology can reach a resolution of a few tens of micrometers with reduced material waste, low manufacturing cost, and processing temperatures. The fabricated devices were printed on glass substrates with silver nanoparticles source and drain electrodes. Minimum sheet resistance of ($0.03\,\Omega/sq$) was achieved by optimizing silver nanoparticles layer thickness. (3,4- ethylenedioxytiophene):poly(styrenesulfonate) (PEDOT:PSS), a low impedance organic semiconductor, was used as channel material. The PEDOT:PSS channel was optimized for a high cross-sectional area to channel length (Wd/L) ratio at $1857\,\mu m$ reaching a maximum corresponding transconductance value of $15.2\,mS$, an order of magnitude improvement on published work. The design was tested with BSA protein and yielded a limit of detection (LoD) of $1\,pM$ with a linear response in the region between $1\,pM$ to $10\,\mu M$, well within the clinically relevant concentrations of BNP and NT-proBNP in blood. This study shows the potential of inkjet printing for fabricating low cost, high performance OECT-based point-of-care biosensors.

Contents

List of Figures

List of Tables

Chapter 1

Introduction

Cardiovascular diseases are one of the leading causes of death across the world [1, 2, 3]. One of the most significant clinical manifestations of the disease is heart failure (HF) [4]. Heart failure is a condition where the heart is unable to fill or pump enough blood to meet the demand of body organs for blood and oxygen. HF is accountable for the highest rates of mortality, morbidity, and healthcare costs among the other forms of Cardiovascular diseases. The current global prevalence of HF is 64.34 million cases accounting for 9.91 million years lost due to disability (YLDs) and 346.17 billion USD expenditure [5]. The clinical symptoms of HF include palpitations, fatigue, dyspnea, and edema [6]. However, these symptoms are not specific to HF and are often associated with respiratory infections especially for elderly patients [7, 8]. This would affect diagnosis, prognosis, and disease management, which could result in serious health issues. Because of these issues, research has focused on a better understanding of the disease at the molecular level by monitoring the concentration of specific biomarkers secreted by cardiac cells into the blood. B-type natriuretic peptide (BNP) and its amino terminal prohormone (NT-proBNP) are two of the most prominent biomarkers. They are peptide hormone that is released in response to volume expansion and the increased wall stress of cardiac myocytes, mainly in the ventricles [9]. It has been well-investigated

that BNP and NT-proBNP can rise in the early stages of HF [10, 11]. BNP and NT-proBNP Have relatively high diagnostic and prognostic value, with a slight edge given to NT-proBNP for its longer half-life period and higher stability in vitro [12, 13]. Current NT-proBNP testing is restricted to immunoassay-based laboratory tests that are done in central labs, which increases the sample processing and results reporting time up to days, not to mention the increase in cost of screening [14]. While the false diagnosis of HF could lead to undertreatment, delayed diagnosis of HF can result in delayed treatment or possibly, false treatment, increased length of stay in hospitals, increased cost, and possible permanent heart damage, which could lead to death [8]. Therefore, there is a need for a reliable, highly sensitive, and real-time point-of-care system that allows for accurate measurement of NT-proBNP, providing results within minutes of sampling in the clinic. Several biosensor designs have been developed to tackle this issue through implementing photonic, biochemical, and electrochemical approaches. Although photonic approaches, such as surface plasmon resonance (SPR) biosensors, may have superior sensitivity and low response time, they suffer from an extremely high cost of material and manufacturing. Biochemical sensing on the other hand is not as expensive as its photonic counterpart, but suffers from the relatively low response time and the need of expertise to operate the devices. With sensitivity, cost, and response time being the most important factors for point-of-care diagnostics and prognostics, electrochemical means of biosensing proved to be the most suitable form of biosensing. The emergence of organic electronics has placed the field of biosensing at an interesting point in time, where novel organic materials are revolutionizing bioelectronics and biotechnology. In this thesis, one of these emerging technologies, the organic electrochemical transistor (OECT) design, is analysed, developed, and optimized using inkjet printing, a novel fabrication technology based on Drop-on-Demand (DoD) additive manufacturing. This technology provides a scalable, repeatable, and reliable method for developing high sensitivity biosensors.

Chapter 2

Literature Review

2.1　HF-Specific Cardiac Biomarkers

Several HF-related biomarkers have been extensively researched and assessed for potential use in clinical settings. Table 2.1 shows the clinical relevance and utility of BNP as compared to other promising cardiac biomarkers [15]. The most prominent biomarkers in clinical practice, other than natriuretic peptides, are C-reactive protein (CRP), cardiac troponins (cTn), tumor necrosis factor (TNF), myeloperoxidase, copeptin, procalcitonin, soluble suppression of tumorigenicity 2 (ST2), among others [16]. Cardiac troponins are a sign of myocytes injury, necrosis, left ventricular hypertrophy (LVH), and systolic dysfunction [17]. Whereas cTn and TNF are inflammatory biomarkers highly correlated to the severity of HF [18]. Myeloperoxidase serves as an oxidative stress biomarker that predicts the mortality risk and other cardiac events in HF patients. Copeptin is a marker of neurohormonal activation and exhibits elevated levels in HF patients. It is a hormone with antidiuretic and vasoconstrictive properties. Recent studies have confirmed the effectiveness of Copeptin in predicting death and its value in guiding therapeutic interventions among HF patients [17]. Procalcitonin is used to distinguish between HF-related dyspnea and non-cardiac related dyspnea. Soluble ST2

Table 2.1: Comparison of promising cardiac biomarkers. Adopted from [6]

Cardiac Biomarker	Pathophysiological Model	Cut-off Value	Diagnosis	Prognosis	Specific
BNP	Cardiac Myocyte Stress	400 pg/mL	+	+	Yes
NT-proBNP	Cardiac Myocyte Stress	0.252 ng/mL	+	+	Yes
MR-proANP	Cardiac Myocyte Stress	120 pmol/L	+	+	Yes
Troponins	Myocyte Injury and Necrosis	0.010.1 ng/mL	+	+	Yes
Copeptin	Neurohormonal Activation	-	-	+	No
Myeloperoxidase	Oxidative Stress	350 ng/mL	-	+	No
NGAL	Renal Dysfunction	-	-	+	No
CRP	Inflammatory	3*103 ng/mL	-	+	No
TNF	Inflammatory	0.0036 ng/mL	-	+	No
sST2	Cardiac Stress, Inflammation, and Fibrosis	35 ng/mL	-	+	No

(sST2) is a biomarker that integrates fibrosis, cardiac stress, and inflammation, providing insightful information on prognosis and risk stratification and management of HF [19, 20].

2.2 Natriuretic Peptides: BNP and NT-proBNP

Incorporating cardiac biomarkers with traditional diagnostic methods have led to some improvement in disease management and risk stratification. However, several reviews of studies on these biomarkers suggest that none can be used as a stand-alone test that guides clinical judgment in diagnosis, prognosis, and therapy [12, 15, 17]. Remarkably for BNP and Nt-proBNP, there had been considerable evidence that supports their use in diagnosis [21] and prognosis [22] with promising studies on the use of natriuretic peptide guided therapy [12]. Recently, the American Heart Association Task Force

on Clinical Practice Guidelines, the Heart Failure Society, and the American College of Cardiology recommended natriuretic peptide biomarker-based screening followed by team-based care as a preventive measure for HF [23]. One of the major strengths of BNP and Nt-proBNP is their high negative predictive value; meaning, if a person tested negative for HF, there is a high probability that he is not experiencing HF [24]. Jourdain et el. published a consolidation of the results of more than six relevant studies that led to a conclusion that introducing BNP and NT-proBNP to clinical judgment increased the accuracy of HS diagnosis to around 71% to 84% [25]. In addition to their role in diagnosis and prognosis, BNP and NT-proBNP demonstrated a potential to be used in managing HF pharmacological strategies and medications. Maisel et al. demonstrated that when used as part of the routine assessment of dyspnea patients, BNP and NT-proBNP assessment have contributed to the decrease in treatment costs and length of hospitalization [26]. Based on what was presented, one can confirm that BNP and NT-proBNP outclass other HF biomarkers with high concentrations in blood being directly correlated to acute and chronic HF in addition to mortality rates in patients [27].

There are several approaches to detect BNP and NTproBNP from blood, summarized as follows:

- Radioimmuno assays: use of a competitive interaction between radioactively labeled antigens and target antigens in binding to available immobilized antibodies (Abs)[28].

- Fluorescent-based Immunoassays: it uses fluorescent molecules, termed probes, that are conjugated to the antibodies. This requires expensive instruments, trained scientists, and fluorescent labeling [29].

- ELISA: enzyme-linked immunosorbent assay (ELISA). Here, the antibodies are linked to an enzyme that catalyzes a specific reaction on a substrate. After the antibodies are bound to the BNP, the substrate is introduced to allow for its

catalyzed reaction, which produces a color change that is then used to quantify the molecule of interest. ELIZA suffers from a number of limitations such as the need for a large sample volume, long detection time of about four hours, expensive instrument cost, and due to the quantification method that is based on color detection, it is not able to detect small levels of BNP [6].

- ECLIA: electrochemiluminescent immunoassay (ECLIA) quantifies the emission of photons by the relaxation of electrons from high energy levels. It is characterized by sensitivity, specificity, miniaturization possibility, and automated operation. However, as previous immunoassays, it still requires expensive and large analytical instruments, operating personnel, and delayed response time [30].

While these assays provide high sensitivity and selectivity for natriuretic peptides, they fail to achieve real-time monitoring of the patients cycles throughout the day [8]. Moreover, testing for BNP and NT-proBNP is still done in medical laboratories where conventional immunoassay-based tests are used. The results may take several hours or even days to be delivered. However, immediate diagnosis of heart failure is crucial to ensure early and appropriate therapy. Hence, the need for a rapid, easy to use, cost-effective, and highly sensitive detection modality is needed. Although there isn't a clear advantage of NT-proBNP over the BNP, recent studies have shown that BNP has a shorter half-life, which may affect the analysis [31]. Additionally, NT-proBNP is shown to be a more selective marker of an early systolic left ventricular dysfunction [32].

2.3   Biosensors for BNP Detection

Biosensors convert the presence of an analyte into a detectable signal representing the level of a biomarker. The main focus in biosensing is transducing the concentration of an analyte to a detectable signal using different detection paradigms. These paradigms

include, but not limited to, electrochemical and optical biosensors. We are going to focus on the electrochemical transduction modality. With considerably high sensitivity and specificity, increased miniaturization, electrochemical transduction has emerged, in the last decade, as one of the most promising sensing modalities [33]. There are four types of electrochemical biosensors; namely: potentiometric, amperometric, impedimetric, and conductometric.

2.3.1   Potentiometric Biosensors

Potentiometric sensors measure the current change of a transistor working in aqueous conditions in response to the change in its gate surface charge. The logarithmic relation between this charge and the concentration of the analyte that binds to the immune-functionalized gate or channel is what is used to measure this concentration. The well-established semiconductor fabrication technology, with its remarkable miniaturization, makes potentiometric sensors a suitable option for point-of-care diagnostics. Recently, several biosensors with clinical applications have been developed for the early detection of diseases [6]. Table 2.2 lists some of the potentiometric biosensors designs and the event they detect.

Lei et al. proposed an enhancement on the potentiometric immuno-sensor design to detect BNP from whole blood. Platinum nanoparticles (PtNPs) were deposited on reduced graphene oxide (rGO) in order to amplify the electrical signal by facilitating electron transfer while providing a higher surface area. The anti-BNP antibodies were, in turn, immobilized on the PtNPs. The design is illustrated in Figure 2.1A. Upon adding different concentrations of BNP, the IV characteristics were obtained (Figure 2.1B), and Linear responses were found in the dynamic range of 100 fM - 1 nM [34].

Table 2.2: Overview of some potentiometric biosensors.

Channel Material	Channel Dimensions	Performance	Detected Event	Reference
rGO	-	$100\,fM$	BNP	[34]
TIPS Pentacene	$W/L = 5.5\,cm/140\,\mu m$	$I_{ON/OFF} = 10^3$	-	[35]
SWCNT	$W/L = 12.5\,\mu m/0.8\,\mu m$	$I_{ON/OFF} = 10^6$	-	[36]
Graphene	-	$10\,cfu/mL$	E. coli bacteria	[37]
Graphene Oxide	$W/L = 2\,mm/2\,\mu m$	$10^4\,cfu/mL$	E. coli bacteria	[38]
Graphene	-	$0.45\,nM$	Zika virus	[39]
PEDOT:PSS	$W/L = 38\,\mu m/24\,\mu m$	$I_{ON/OFF} = 1.74 \times 10^5$	Action potential	[40]
PEDOT:PSS	$W/L = 5\,mm/1\,mm$	$0.01\%BAC$	Ethanol in breath	[41]
PEDOT:PSS	-	$LOD = 0.1\,mM$	Glucose	[42]
PEDOT:PSS	$W/L = 6\,mm/100\,\mu m$	$LOD = 5\,nM$	Dopamine	[43]
PEDOT:PSS	$W/L = 6.0\,mm/0.2\,mm$	$LOD = 0.1\,nM$	Epinephrine	[44]
PEDOT:PSS	$W.d = 1\,mm.100\,nm$	$LOD = 0.5\,\mu M$	Cell death	[45]
PEDOT:PSS	-	$LOD = 10\,pM$	cDNA	[46]
PEDOT:PSS	$Wd/L = 200\,\mu m \times 80\,nm/6\,mm$	$LOD = 0.1\,nM$	cDNA	[47]
PEDOT:PSS	-	$LOD = 1\,pg/ml$	PSA	[48]

2.3.2 Amperometric Biosensors

The sensing modality in amperometric sensors relies on measuring the current change due to redox reactions and electron transfer on the surface of their working electrodes. Because of their successful implementation in many biosensing platforms such as glucose biosensors, amperometric biosensors have been highly researched and used in commercial products [33]. Unlike potentiometric sensors, the analyte concentration is linearly related to the current response, which is a major advantage of amperometric sensors over potentiometric sensors. However, The most challenging disadvantages of amperometric enzyme-based biosensor detection is signal depletion from bio-fouling agents and interference from other chemicals present in the sample matrix. It is also challenging to find the right enzymatic biochemistry of antigens and Abs in immuno-sensing applications like BNP detection. This requires an additional indirect electrochemical immunoassay to provide electroactive species to transfer electrons in redox reactions, which adds to the complexity of the design. The measurement makes use of the linear relationship between
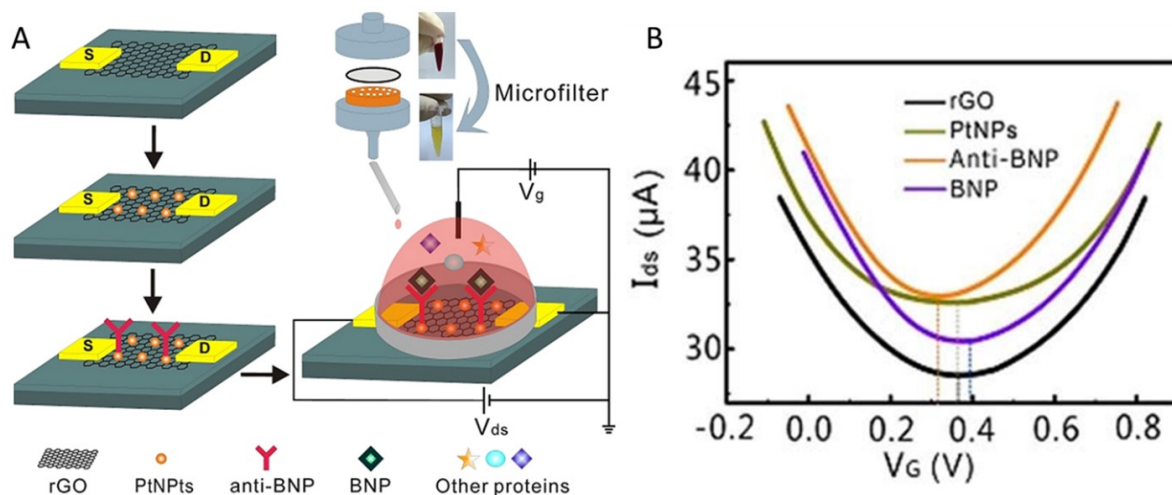
Figure 2.1: A) Schematic illustration of the PtNPs-decorated rGO FET biosensor with a custom made microfilter for BNP detection. B) Plots of transfer curves at Vds=100 mV for the FET biosensor in the process of rGO formation, PtNPs decoration, anti-BNP immobilization, and BNP binding. Adopted from [34].

the current resulting from the redox reaction and the concentration of the analyte. The transfer of electrons could be enhanced by using Redox mediators that undergo intermediate redox reactions. Moreover, incorporating nanomaterials can further enhance the performance of amperometric biosensors. Serafin et al. presented another approach for using a sandwich-type immunoassay in designing a disposable amperometric sensor, as seen in Figure 2.2A. Peroxidase-labeled detector Abs were immobilized on gold nanoparticles grafted carbon electrode. The sensor response, obtained by voltage measurements after incubation of 45 minutes, showed a linear response to the BNP concentration in the range between 0.014 and 15 ng/mL with a LOD of 4 pg/mL, as seen in Figure 2.2B. The validity of the selectivity was done by testing against cTnI, CRP, cTNT, L(a), Interleukin (IL)-8, TNF alpha, NTproBNP, and receptor tyrosine kinase AXL biomarkers [49].
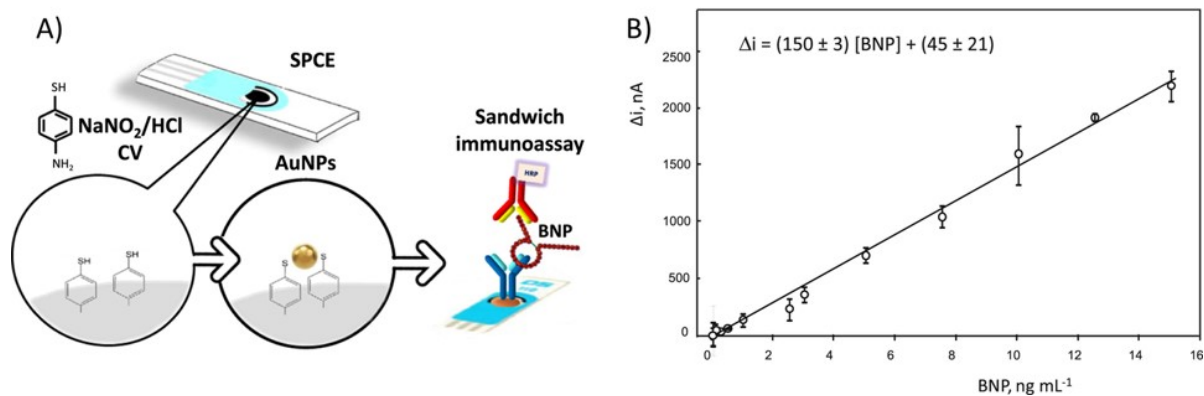
Figure 2.2: A) Schematic representation of developed amperometric BNP biometric. B) Calibration plot constructed for the amperometric determination of BNP at the HRP-anti-BNP-BNP-anti-BNP-AuNPs-S-Phe-SPCE immunosensor.Adopted from [49]

2.3.3 Impedimetric Biosensors

Impedance-based electrochemical biosensors employ an equivalent circuit model for the sensor interface. This model is composed of resistive, capacitive, and inductive components that give rise to a total characteristic impedance, which is altered depending on what adheres to the sensing surface. Electrochemical Impedance Spectroscopy (EIS) is used to monitor the changes of the interface impedance when the analyte binds to the functionalized surface. Selvam et al. developed an NT-proBNP non-faradaic impedimetric sensor that was built on a printed circuit board (PCB). Low limit of detection was achieved by leveraging the size matched confinement design of the electrode design. they demonstrated the sensor performance with EIS and fixed frequency plot. They were able to achieve a limit of detection of around the $10fg/mL$ range [50].

2.3.4 Conductometric Biosensors

The working principle of conductometric immuno-sensors makes use of measuring the change in conductance due to the change of the type and quantity of ionic species in the solution in response to the analyte binding to the immobilized antibodies. Conductance measurements are done in the presence of an applied electric field. It is worth mentioning

that the large influence of the solutions ionic content and the nonspecific adsorption impact on conductometric biosensors hindered their further development.

2.4   Transistor-based Sensors

When developing a point-of-care diagnostic system, ease of manufacturing, and cost per unit play a crucial role in the design process. Although silicon-based devices are widely applied in many areas of technology, noteworthy progress in the fabrication methodology of organic transistors led the researchers to utilize various substrates, such as plastic [51], glass [52], and fiber [53]. The OTFTs fabricated on flexible substrate and glass, demonstrated comparable characteristics to the amorphous silicon hydrogenated (a-Si:H) TFT [54]. With the high demand on high-end electronic devices, the OTFTs are being integrated into economically vital and high-end applications, such as flat panel display, light-emitting diode (LED) [55], radio frequency identification (RFID) tag [56], sensors [57], static random access memory (SRAM) [58], and flexible integrated circuits [59]. Figure 2.3a compares their performance and cost characteristics. Though the performance of organic transistors is not comparable to the silicon transistor, it still finds utilization in certain innovative applications that are not possible with conventional semiconductors, or if feasible, they are too expensive to be realized commercially [60]. When comparing OECTs and OFETs, the two major sub-classes of OTFTs, in a gain versus bandwidth perspective, as seen in Figure 2.3b, the transconductance of OECTs is larger than that of OFETs up to a certain frequency, beyond which OFETs have the performance advantage. This Transconductance superiority of OECTs makes them ideal for sensing biosignals since they are, in fact, of a lower frequency range [61].
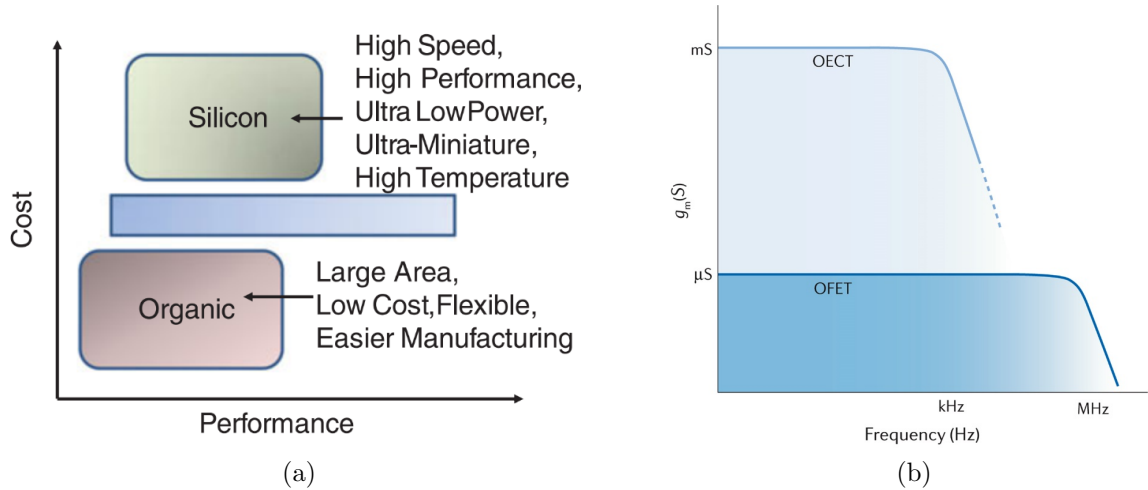
Figure 2.3: (a) Cost versus performance of organic and inorganic semiconductors. Adopted from [60]. (b) Comparison between organic electrochemical transistors and organic field-effect transistors. Adopted from [61]

2.4.1 Organic Electrochemical Transistors

Organic Electrochemical Transistors (OECTs) are thin-film transistors with a structure similar to that of an organic field-effect transistor (OFET). However, OECTs use an electrolyte between the channel and gate rather than a conventional dielectric with dipoles. OECTs and OFETs represent the opposite ends of the same spectrum in terms of the operating mechanism. They share many properties and are similar in terms of materials, processes, and form factors. However, OECTs are a considerably less mature technology than OFETs. Moreover, OECTs have a simpler structure, are stretchable, and operate at relatively low voltages. this has prompted the scientific communities to design several types of OECT-based bioelectronic devices to sense DNA [46], hormones [62], metabolites [63], neurotransmitters [43], cells [64], biomarkers [48], or to monitor cellular [65, 66], tissues [67], or brain activities [68].

Among a number of soft organic materials, poly(3,4-ethylenedioxythiophene)poly-(styrenesulfonate) (PEDOT:PSS) has been one of the most employed channel materials for biological and chemical sensing [69], as well as other bioelectronic devices (ref our

12

paper on biodegradable electrode array). PEDOT:PSS is composed of two components: polystyrene sulfonate, which carries a negative charge, and poly(3,4- ethylenedioxythiophene), which is based on polythiophene and carries a positive charge. Figure 2.4 shows the chemical structure of $PEDOT^+$ and PSS^-. PEDOT is an organic semiconductor degenerately doped p-type by PSS to reach conductivities as high as 1,000 S/cm [70]. PEDOT:PSS is able to conduct both electrons and ions [71]. When the PEDOT:PSS film is in contact with an electrolyte, the ions (predominantly cations) from this electrolyte enter the PEDOT:PSS film, and the conduction of the material increases. Equation 2.1 shows the doping/de-doping of PEDOT:PSS. By application of a small positive gate voltage, cations from the electrolyte enter the PEDOT:PSS film and reduce the PEDOT component to its neutral state (direction from left to right in equation 2.1).

$$PEDOT^+ : PSS^- + M^+ + e^- \longleftrightarrow PEDOT^0 + M^+ : PSS^- \qquad (2.1)$$
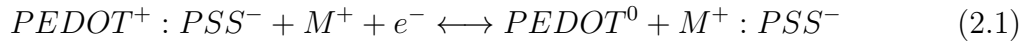
Where M^+ is a cation in the electrolyte and e^- is an electron. This results in the electrochemical de-doping of the PEDOT:PSS film, thus in the decrease of the channel current. The density and mobility of the holes have an influence on the electronic transport. The ions in the electrolyte determine the ionic transport [72]. The reduction of the highly conducting form of $PEDOT^+$ to the less conducting form of $PEDOT^0$ is reversible. The reduction of the PEDOT:PSS film is operated by the migration of cations into the channel. When a small positive gate voltage is removed, the cations diffuse back into the electrolyte [73] (direction from right to left in equation 2.1).

Theory of Operation

Despite the significant differences between OECTs and MOSFETs, OECTs can be described by models for MOSFETs as long as the interfacial capacitance used to describe MOSFETs is replaced by a volumetric capacitance for OECTs [74]. where Equation 2.2
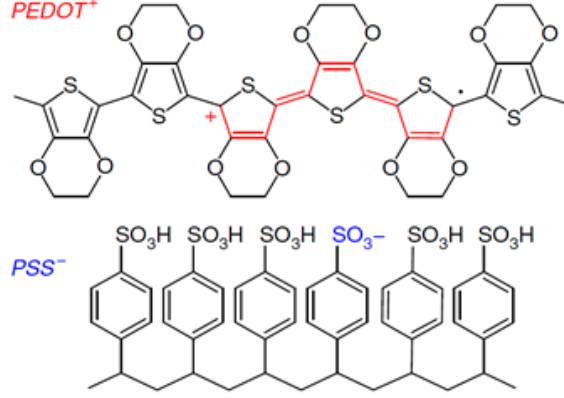
Figure 2.4: Chemical structure of PEDOT and PSS.

describes the relationship between the drain current I_{ch}, the gate-source voltage V_{GS} and the drain-source voltage V_{DS} in linear and saturation regimes, respectively. C^* is the volumetric capacitance per unit volume, μ is the carrier mobility in the semiconductor, W, d, and L is the channel width, thickness, and length of the OECT, respectively [75].

$$I_{ch} = \begin{cases} \mu C^* \frac{Wd}{L}(1 - \frac{V_{GS} - \frac{V_{DS}}{2}}{V_{th}})V_{DS}, & \text{for } V_{DS} > V_{GS} - V_{th} \text{ (linear regime)} \\ \\ -\mu C^* \frac{Wd}{L}(\frac{(V_{GS} - V_{th})^2}{2V_{th}}), & \text{for } V_{DS} < V_{GS} - V_{th} \text{ (saturation regime)} \end{cases} \tag{2.2}$$

Because the charge carrier density in the semiconductor is a function of the gate-source voltage, the drain current can be modulated by adjusting the gate-source voltage. This modulation of the drain current (output current) with the gate-source voltage (input voltage) is quantitatively described by the most fundamental field-effect transistor parameter, the transconductance (g_m):

$$g_m = \frac{\partial I_D}{\partial V_{GS}}\bigg|_{V_{DS}=cte} \tag{2.3}$$

By combining equations 2.2 & 2.3, the following expressions for the transconductance

in the linear and saturation regimes can be derived:

$$
g_m =
\begin{cases}
-\mu C^* \frac{Wd}{L} V_{DS}, & \text{for } V_{DS} > V_{GS} - V_{th} \text{ (linear regime)} \\[2em]
\mu C^* \frac{Wd}{L} (V_G - V_{th}), & \text{for } V_{DS} < V_{GS} - V_{th} \text{ (saturation regime)}
\end{cases}
\tag{2.4}
$$

Several authors have shown that OECT transconductance is directly proportional to the ratio $^{Wd}/_{L}$, as shown in Figure 10, where the authors compared several channel materials and the corresponding maximum transconductance normalized over the volume of the channel [75]. The fact that transconductance scales with thickness, and not just the width-to-length ratio, distinguishes OECTs from FETs.
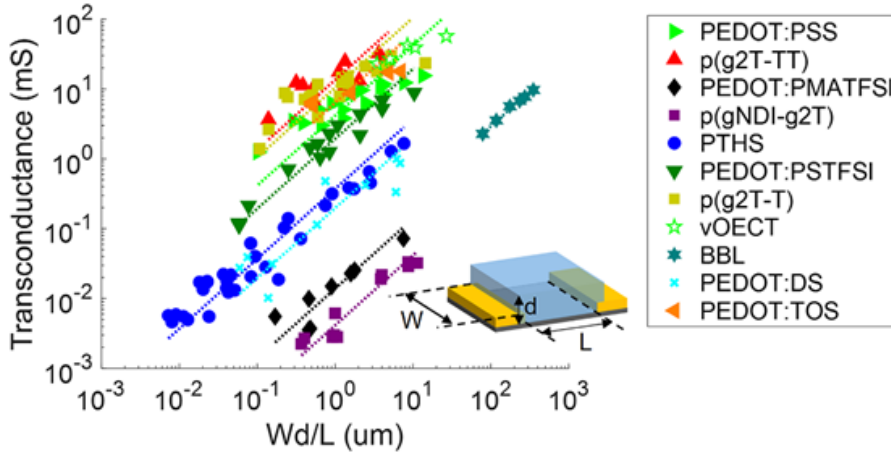
Figure 2.5: Geometry scaling of peak transconductance for different channel materials. Adopted from [75]

This distinction arises because field-effect doping only modulates carrier density at the semiconductor-insulator interface, whereas electrochemical doping modulates carrier density throughout the bulk of the semiconductor, as shown in Figure 2.6[75].
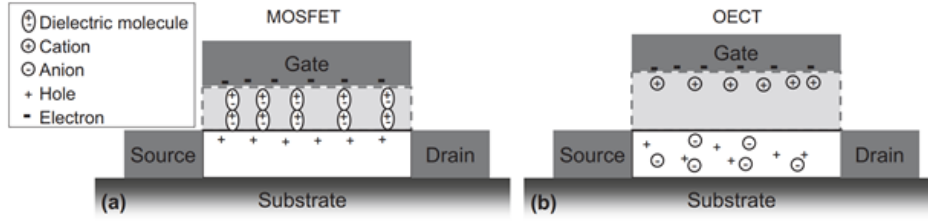
Figure 2.6: Comparison of MOSFET (a) and OECT (b) operation. In both (a) and (b), the white region represents the transistor channel. In (a), the light-gray region with a dashed outline represents an oxide insulator. In (b), the light-gray region with a dashed outline represents an electrolyte. The electrolyte in the OECT contains mobile cations and anions which can penetrate into the OECT channel, whereas the dielectric in the MOSFET contains immobile dipoles.Adopted from [75]

2.5   Fabrication Techniques

fabrication techniques are well-established and commonly used methods for microfabrication of functional OECTs. The fabrication process of the simplest device structure requires gate patterning, dielectric deposition, coating with photoresist, development, deposition of source and drain material, lift-off process, photoresist coating and development, channel width and contact hole development [76]. Figure 2.7 illustrates the fabrication steps of a typical device structure. This process is time-consuming, expensive, and requires a clean room, which limits its integration in less developed countries.

2.5.1   Inkjet Printing

A novel fabrication process that is gaining more visibility is inkjet printing. The inkjet printing process is a drop-on-demand fabrication technique with micron resolution, that it utilizes tiny nozzles to form small droplets of functional materials to directly pattern on a substrate. The resolution and capability of inkjet printing are owed to advances in material dispensing technologies and electronic alignment. This method uses maskless patterns by sequentially depositing multiple layers of different materials without
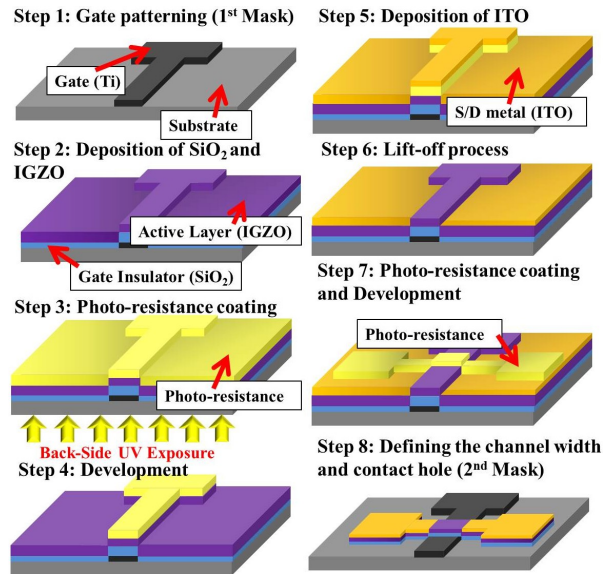
Figure 2.7: Typical thin-film transistors (TFTs) fabrication technique. Adopted from [76]

perturbing the previously deposited layers. This additive manufacturing process makes it possible to deposit a variety of materials counting dielectrics, conductors, and semi-conductors, on a variety of substrates such as organic, flexible, plastic, and papers, in addition to the conventional silicon wafers and glass plates. This ability allows for fast and cost-effective prototyping. The printer used in this work is FUJIFILM Dimatix Inkjet Printer (DMP-2850), which is capable of scaling designs up to 811 inch areas while maintaining micro-level resolution printing. The resolution is controlled by the spacing between individual drops, as illustrated in Figure 2.8a. The drops are jetted out through 16 nozzles of 31x31 Square holes, as seen in Figure 2.8b.

Jetting Waveform

Producing a well-defined droplets is essential for obtaining high-quality micro structures. One of the most important factors in determining the shape of the droplet is the jetting waveform. The jetting waveform is usually divided into several segments, each of which contributes to a specific function.

Figure 2.9 shows the three phases of a basic jetting waveform. The standby phase (phase zero) connects the previous waveform to the beginning of the next, where the piezoelectric element remains deformed in this phase. When the applied voltage halts (phase one), the piezoelectric element relaxes to its original shape, expanding pumping chamber to its greatest capacity. At this phase, the ink fills pumping chamber from the reservoir. Next, a voltage pulse is applied that causes the piezoelectric element to expand (phase two), and consequently, the chamber to be compressed where a pressure is generated to eject the droplet. There is a number of parameters that needs to be precisely set in order to obtain well-defined droplets. These are as follows: Voltage level, pulse width, jetting frequency, and slew rate.

- Voltage level: There is a direct relation between the voltage level and the speed of the droplet. Therefore, controlling this voltage level prevents splashes when the ink droplet hits the substrate's surface. Increasing the voltage level also allows for ejection of inks with high surface tension, which is not possible at lower voltages.

- Pulse width: it is the duration of time where the voltage is applied. Once the droplet is ejected, increasing the pulse width further would slightly increase the drop size to a certain extent, and further increase in the pulse width has little effect on the drop formation procedure.
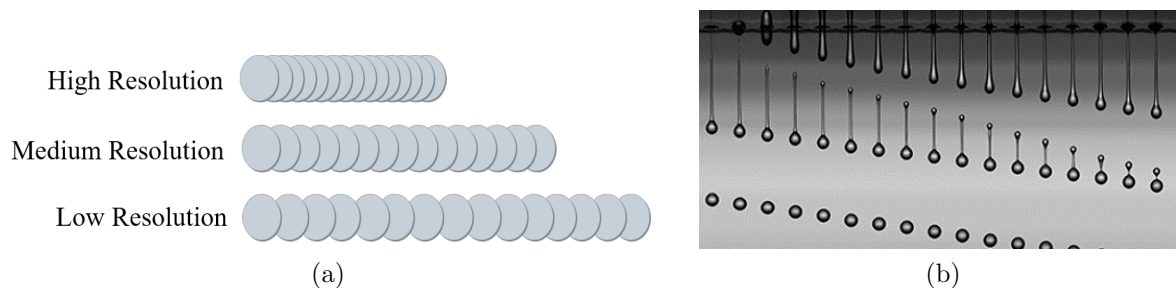
Figure 2.8: (a) Illustration showing the dependence of resolution on drop spacing. (b) High-speed footage of drop formation during jetting. Adopted from Mark Jan van der Meulen/University of Twente.

- jetting frequency: The jetting frequency allows for faster printing. It is however, also dependant of on the viscosity of the liquid. Higher viscosity inks, won't be able to be jetted at high frequencies.

- the slew rate, it has minimal influence on droplet formation, but it determines how quick the volume of chamber changes. This should be optimized for each type of ink used, depending on their viscosity, surface tension, and solid content.
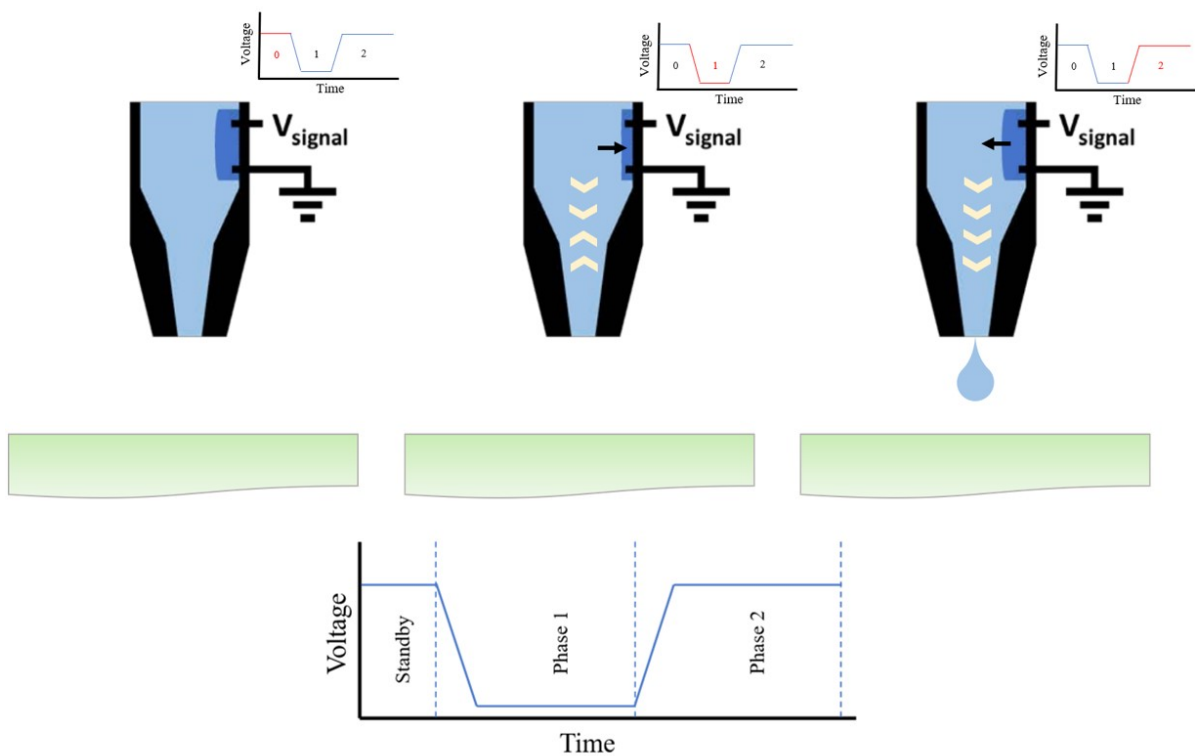
Figure 2.9: Schematic diagram of the response of the print head to the three basic stages of a jetting waveform.

Ejectability Assessment

Ideal jetting waveforms depend mainly on the fluid characteristics. Thus, the waveform can be adjusted, including the number of segments, according to the fluid properties. One way to characterize fluid ejectability is to compute the Z number, the reciprocal of

Ohnesorge number (Oh), is a factor that is mainly affected by the physical properties of the fluid, including viscosity, density, and surface tension. This is given by the equation 2.5:

$$Z = \frac{1}{Oh} = \frac{\sqrt{We}}{Re} = \frac{\sqrt{\rho r \gamma}}{\mu} \qquad (2.5)$$

Where We is Weber number, Re is Reynolds number, ρ is the inks density, r is the diameter of the nozzle, μ is the ink's viscosity, and γ is the inks surface tension. As the value of Z decreases, the forces required to form and eject the droplets increases [77, 78]. Figure 2.10 shows the inkjet printable regime in the Weber-Reynolds plane. A Z-Value between 1 and 10 indicates good printability via drop-on-demand method [78, 79, 80]. A desirable droplet is achieved when a single droplet is ejected, having a distinct circular shape. Satellite droplets could be formed directly after the ejection of the main droplet depending on the primary droplet ejection speed and the length of its thread tail. This is an adverse effect having a large impact on the print quality. However, the jetting voltage and waveform play a major role in minimizing and eliminating this effect [81, 82].
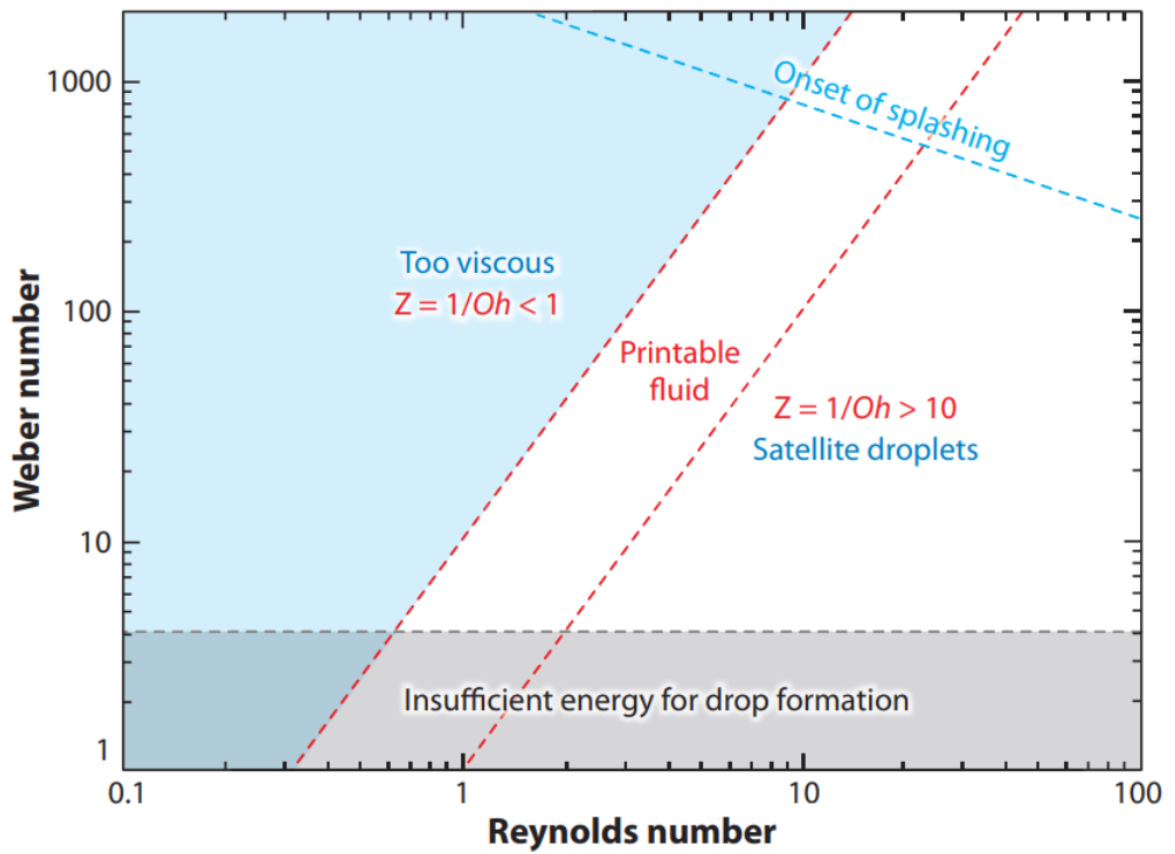
Figure 2.10: Regime of fluid properties where inkjet printing is possible. Adopted from [80]

Chapter 3

Specific Aims

Aim 1: Design, development, and testing of an inkjet-printed OECT.

Hypothesis A: we hypothesize that an OECT can be fabricated on a glass substrate using inkjet printing.

Hypothesis B: we hypothesize that optimizing organic semiconductor formulation would have a significant effect on the volumetric capacitance of the organic semiconductor.

Hypothesis C: we hypothesize that the design and fabrication of an OECT with increase channel volume would increase the transconductance of the Fabricated Transistor.

Challenge: Controlling the printing parameters and their effect on the quality of the print and subsequently the performance of the device.

Approach: using low temperature, high-resolution inkjet printing technology to fabricate OECTs.

Impact: the development of an inkjet-printed, high-performance OECT.

Aim 2: Test the ability of the developed OECT to detect picomolar concentration of BSA.

Hypothesis A: we hypothesize that the optimized OECT can detect picomolar-concentration of BSA.

Challenge: identifying the right parameters that would increase the sensitivity of the biosensor to BSA on the surface of the channel.

Approach: the concentration of the BSA will be controlled in a set of solutions, and will be tested on the optimized sensor design.

Impact: the final design would be a cost-effective, high sensitivity platform for protein detection that can be tailored towards NT-proBNP detection through immobilization of Abs of the protein in question.

Chapter 4

Methodology

Aim 1: Design, development, and testing of an inkjet-printed OECT.

In this aim, we employ a novel fabrication technique that utilizes piezoelectric inkjet printing with micro level resolution to build a high sensitivity NT-proBNP biosensor.

The fabrication process was done using a commercially available material printer (DMP- 2850, Fujifilm Dimatix, USA). The printer is compatible with a piezo-driven 16-nozzle printhead with a chamber volume of either 1 or 10 pL. This unit requires the fluids viscosity and surface tension to be in the range of 10-12 mPa.s, and 28-42 mN/m respectively in order to achieve optimum drop formation. In this work, all the inks properties we optimized through changing the formulation and the solvent-to-solute ratio to achieve the highest possible printing resolution.

4.1 Materials

The source and drain electrodes were patterned using a commercially available silver Nanoparticles (AgNPs) ink. The channel was patterned using a self-developed formulation of PEDOT:PSS ink. The passivation layer was printed using a cross-link between

Table 4.1: Recipes for the PEDOT:PSS-based organic semiconductors

	PEDOT:PSS	Water	DMSO	EG	Triton-X	Graphene
Ink 1 (v/v%)	50%	39%	5%	5%	1%	-
Ink 2 (v/v%)	86%	10%	-	3%	1%	-
Ink 3 (w/w%)	16.67%	-	-	-	-	86.33%

poly(4-vinylphenol) (PVPh) and poly(melamine-coformaldehyde) (PMF). the AgNPs ink used is the JS-B40G, developed by Novacentrix. It was used as is with no modifications since its viscosity and surface tension are already compatible with the Dimatix inkjet printer. This ink has 40 wt% of AgNPs, suspended in diethylene glycol monobutyl ether. Three formulations of PEDOT:PSS were tested. Ink 1 is prepared by diluting the PEDOT:PSS solution with 39% v/v water to achieve good dispersion and prevent nozzle clogging. Dimethyl sulfoxide (DMSO) (472301, SigmaAldrich) was also added with 5% to the total solution; a solvent that enhances the conductivity through screening effect [83]. Ethylene glycol (EG) was added to the mixture in a ratio of 5% to enhance conductivity, through modifying the conformation of the polymer from a coil to a linear structure by moving towards Quinoid structure from Benzoid structure as seen in figure 4.1 [84]. 1% v/v of TritonX (Sigma-Aldrich), which is a surfactant, is added to modulate the surface tension of the mixture to fall in the required range of the printing process as well as increasing the conductivity of the solution [85]. Ink 2 is prepared from 86% PEDOT:PSS solution with 10% v/v water, 3% Ethylene glycol (EG), and 1% v/v of TritonX. Ink 3 was a commercially available blend of PEDOT:PSS and Graphene (900442, Sigma-Aldrich) in a ratio by weight of 5:1. Table 4.1 summarizes the three studies mixtures of PEDOT:PSS.

The viscosity of the optimized solution was measured and confirmed using a rotational viscometer (FungiLab). Annealing of the printed PEDOT:PSS structures are done on a hotplate at 180 °C for 1 hour.

The Dielectric layer is composed of a polymer-based ink. It was formulated using

Benzoid structure   Quinoid structure
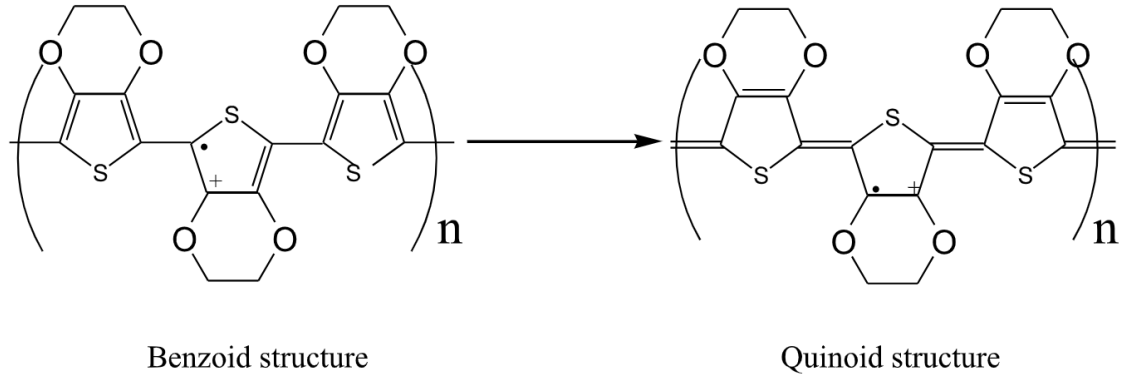
Figure 4.1: Scheme of transformation of the PEDOT chain from the benzoid to the quinoid structure. The dot and plus represents the unpaired electron and positive charge on the PEDOT chain, respectively. Adopted from [84]

Table 4.2: Fluid properties of the used inks at room temperature

Material	Nozzle Diameter (μm)	Density (g/cm^3)	Viscosity ($mPa.s$)	Surface Tension (mN/m)	Z Number
AgNPs	21.5	1.56	17.2	31	1.874709
PVPh	21.5	0.956	12.8	29.3	1.917221
PEDOT:PSS-ink 1	21.5	1.09	9.3	33.32	3.004706
PEDOT:PSS-ink 2	21.5	1.05	12.4	36.2	2.305401
PEDOT:PSS-ink 3	21.5	1.0012	8.08	39.57	3.612029

1-Hexanol as a solvent material with a 17:1 w/w% ratio, between 1-Hexanol and the polymers. The recipe is composed of PVPh (436216, SigmaAldrich) and PMF (418560, Sigma-Aldrich) with 1:1 w/w% ratio [86]. This formulation has inkjetable properties that permitted a proper droplet formation without satellite droplets. The printed layer was then cured using the overhead UV-light of the printer to allow crosslinking. The chemical structure of PVPh and PMF as well as their crosslinking is shown if figure 4.2A, B, and C, respectively. A comprehensive overview of the fluid properties of the used inks is shown in table 4.2.
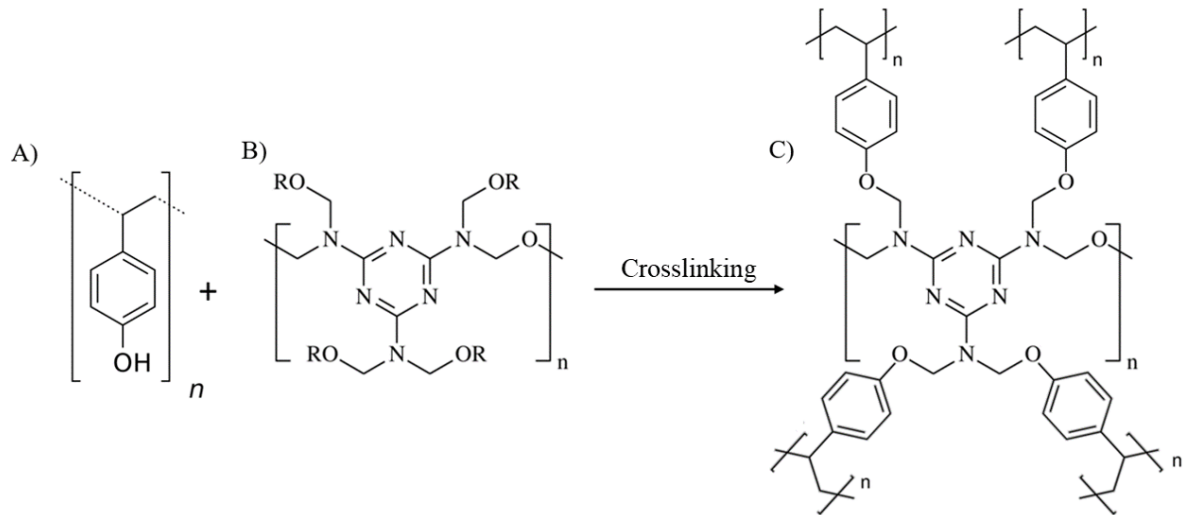
Figure 4.2: Chemical structures of A)PVPh, B)PMF, C)Crosslinked PVPh/PMF

4.2 Fabrication Process

4.2.1 Role of the Substrate

The substrate is a crucial component of printed electronics. It serves a number of purposes such as structural support to the overlying layers. It also takes part in modulating the electrical performance of the printed devices. In this section, several effects and characteristics of the substrate are introduced and discussed. The first is the characteristic of the substrate that effects printing quality is the interaction between ink and substrate. The adherence of ink onto the substrate is heavily dependent on the chemical interactions established at the interface. A straight forward method for evaluating these interactions is the contact angle of the ink droplet on the substrate. This characteristic is most noticeable on substrates with very small droplet contact angles where leeching and pattern boundary stability is weak. To improve these metrics, operations, such as plasmonic surface activation and acetone treatment, are available. The working principle of these treatments is that they clean the surface from any contaminant that might be on the surface in addition to grafting hydroxyl group on the surface, which make the

27

surface hydrophilic. Though surface optimization can improve ink-substrate interaction, there are external effects separate from the substrate, such as ink solvent evaporation, that may enhance or diminish print quality. To maximize the print quality and maintain a cost-effective design, gold-seal glass slides (Thermo Scientific) were primarily used as substrate. A 4-step cleaning process using different solvents was utilized to enhance the The surface hydrophilicity of the glass. The order of the solvents used was as follows: acetone, ethanol, isopropanol, and de-ionized water.

4.2.2   Inkjet Printing

After undergoing a deep cleaning cycle, the glass substrate becomes ready for printing. The first layer is the silver source and drain (figure 4.4a). The commercially available AgNPs inks are stabilized by coating them with a stabilizing, non-conductive agent. During the thermal sintering process, the coating degrades and the individual particles coalesce to form larger particles, making the structure conductive as seen in figure 4.3. This phenomenon happen at temperature of 250 °C. Printing the first layer, which includes the source and drain of the OECT, was done using drop spacing of 35 μm. The number of layers of silver forming the source and drain of the OECT has been chosen to reflect the lowest sheet resistance, while keeping the designed dimensions of the printed structures. After that, the PVPh insulation layer is printed above the source and drain
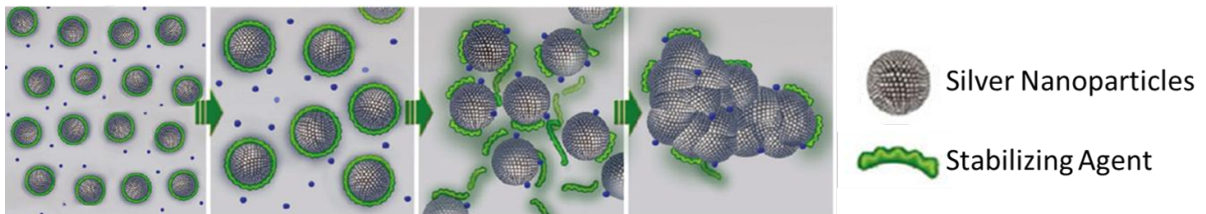
Figure 4.3: Schematic illustration of the sintering process of AgNPs. Adopted from [87]

leads (figure 4.4b). Curing of this layer is done using the printhead UV-light accessory. The UV LED is turned on automatically while the printhead is printing individual lines.

Table 4.3: Inkjet-printing deposition parameters per ink.

Parameter	AgNPs	PVPh	PEDOT:PSS ink 1	PEDOT:PSS ink 2	PEDOT:PSS ink 3
Printhead	DMC-11601	DMC-11610	DMC-11610	DMC-11601	DMC-11601
Drop Volume (pL)	1	10	10	1	1
Number of Active Nozzles	1	1	2	2	2
Print Resolution (dpi)	846.67	725.71	1270	1270	1270
Drop Spacing (μm)	30	35	20	20	20
Printhead Temp (°C)	25	25	25	25	25
Platen Temp (°C)	25	35	25	25	25
Jetting Voltage (V)	25-30	25-30	25-35	25-35	25-35
Jetting Frequency (kHz)	4	4	3	3	3
Printing Distance (μm)	40	400	400	400	400

This ensures a somewhat uniform formation of the cross-linked PVPh film. No further heat treatment is applied to the PVPh films. Following he printing to the passivation layer, the organic semiconductor layer is printed (figure 4.4c). As mentioned previously, this layer is composed of a mixture of PEDOT:PSS and EG forming the organic semiconducting (OSC) channel of the OECT. A schematic of the Fabrication steps is shown in figure 4.4. As seen previously, each ink has different fluid properties, therefore, the printing parameters of each ink have been optimized to produce the highest print quality. These parameters are shown in table 4.3. Each waveform were optimized in pulse duration, pulse level, and slew rate to best fit the fluid properties of each ink. The optimized waveforms for each ink are shown in 4.5
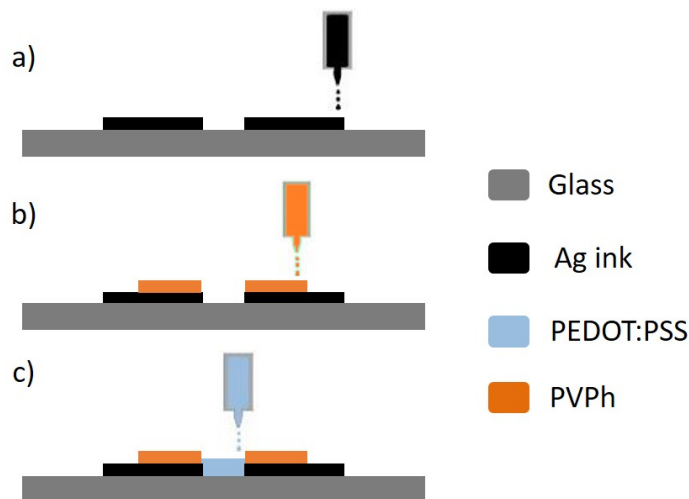
Figure 4.4: The fabrication process of inkjet-printed OECTs.

4.3 Electrochemical Characterization

The electrochemical characterization of the three developed PEDOT:PSS inks was performed with a Potentiostat/Galvanostat/ZRA system (Gamry Instruments, USA) employing a three-electrode cell. Phosphate buffer saline (PBS) was used as the electrolyte medium, with a 3D-printed well holding it in place. A platinum (Pt) electrode was used as a counter electrode while Ag/AgCl wire was used as a reference electrode. A schematic of the EIS setup is shown in figure 4.6a. Several electrode volumes where fabricated using the same inkjet printing technology. a schematic of the fabrication steps is shown in figure 4.6b.

The fabricated electrodes characterized using electrochemical impedance spectroscopy (EIS) to examine ion-mediated carrier modulation in the three PEDOT:PSS films. The impedance spectrum was fitted using the electrode model developed by Ryu et al. as shown in figure 4.7. Several components are involved in the circuit mode of the electrode/electrolyte interface. These are as follows:

- Solution resistance (R_s): solution resistance is the resistance between the reference electrode and the working electrode in an electrolyte solution. For the designed

30
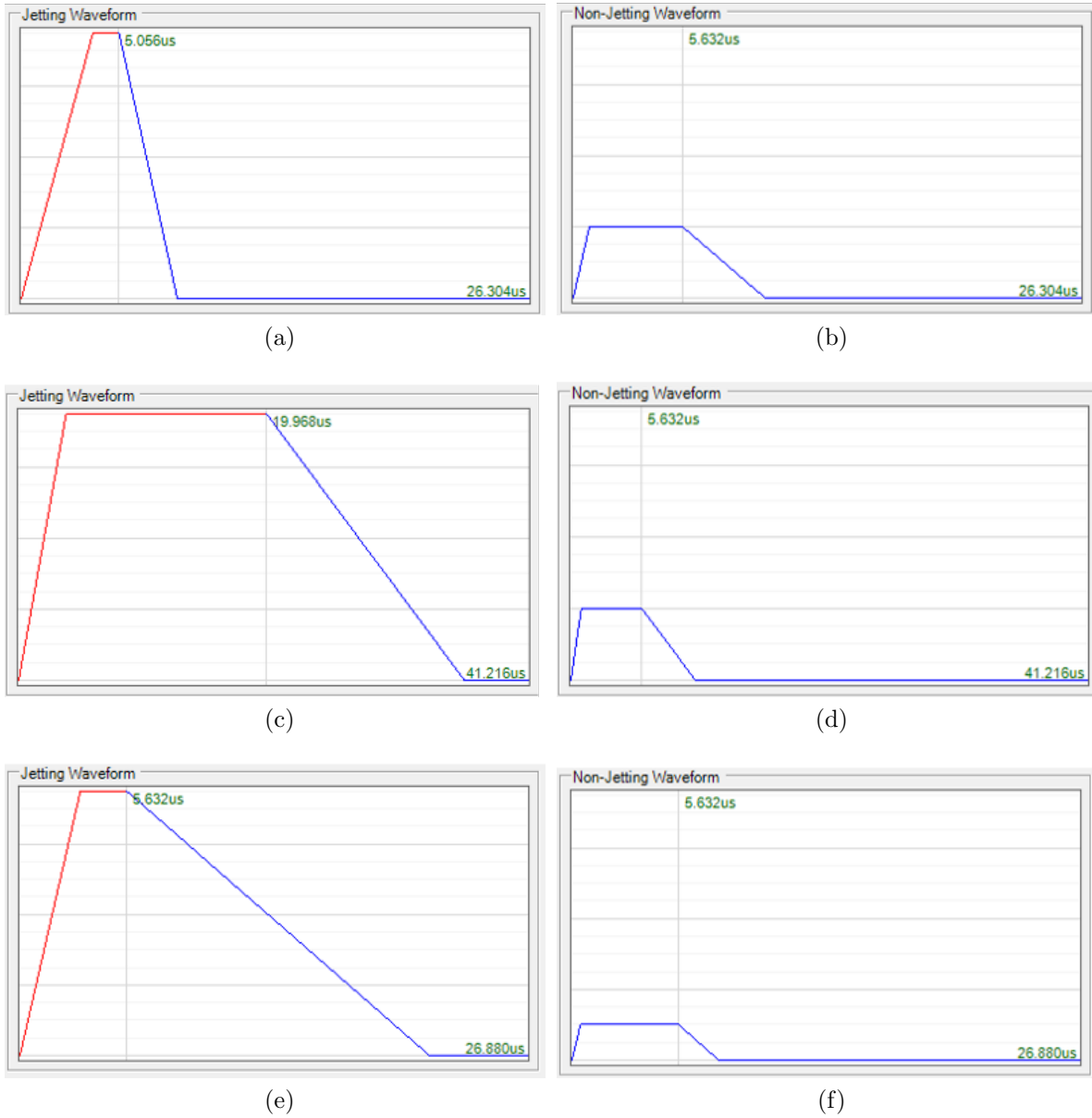
Figure 4.5: Tailored jetting and non jetting waveforms for (a&b) Novacentrix JS-B40G ink , (c&d) PVPh ink, and (e&f) PEDOT:PSS inks
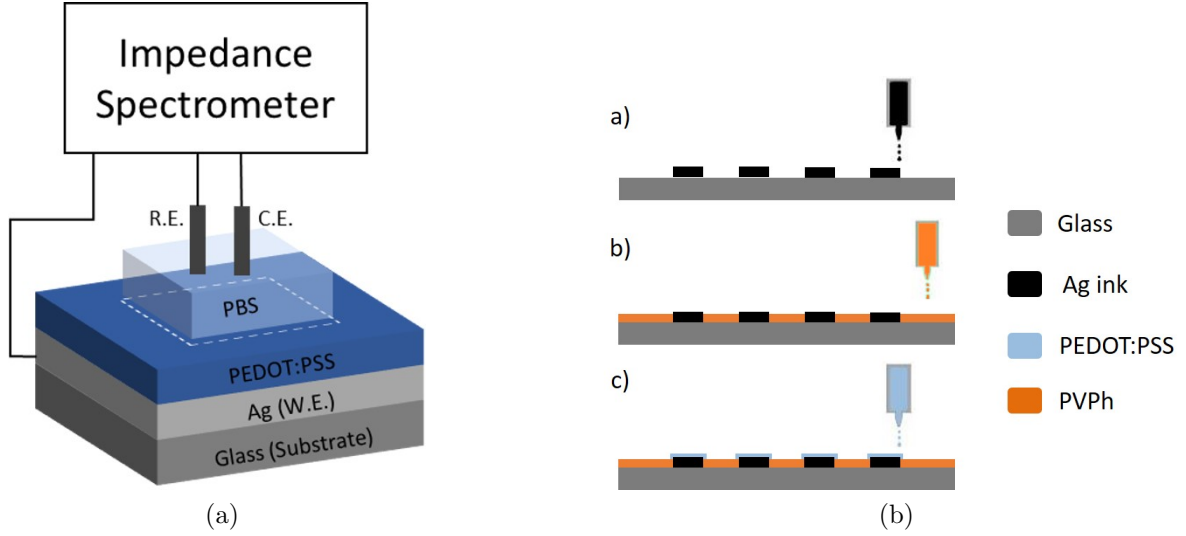
Figure 4.6: (a) EIS setup. (b) fabrication process of inkjet-printed OECTs.

flat electrode, R_s can be simply described by the following equation:

$$Z = \frac{\rho}{4r} \tag{4.1}$$

where, is the solution resistivity and r is the radius of the electrode

- Coating capacitance (C_c): Coating capacitance is developed where the electrodes are separated by a dielectric medium. Here, the (C_c) was formed by coating of PEDOT:PSS on the surface of the electrode. The C_c is given by:

$$C_c = \frac{\epsilon_0 \epsilon_r A}{d} \tag{4.2}$$

where ϵ_0 is the dielectric permittivity of free space, ϵ_r is the relative dielectric permittivity of the medium between the two plates, d is the distance between them, and A is the surface area of the electrode site. C_c is also proportional to the surface area of the electrode. The coating capacitance was extracted for different electrode areas to calculate the volumetric capacitance of the OECTs.

- Pore resistance (R_{pore}): Pore resistance is formed when ionic conduction paths are generated through the PEDOT:PSS coating layer. It is defined as:

$$R_{pore} = \frac{\rho d}{A_p} \tag{4.3}$$

where, ρ is the solution resistivity, d is the length of the pore, and A_p is the total surface area of the pore.

- Double layer interface impedance (Z_{CPE}): this element account for the Electrical Double layer (EDL) formed at the electrode electrolyte interface. A constant Phase Element (CPE) is usually incorporated in this impedance to model the capacitive effects in the EDL since this element can compensate the impact of the distributed time constants.

- Charge Transfer Resistance (R_t): this resistance emerges from the inefficient redox reaction at the electrode surface.

- Finite Diffusion Impedance (Z_T): The diffusion process of ionic species at the electrode/electrolyte interface leads to generation of this type of impedance.
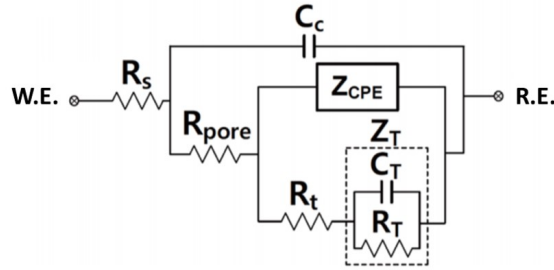
Figure 4.7: Equivalent circuit model of the PEDOT:PSS electrodes. Adopted from [88].

4.4 Electrical Characterization

4.4.1 Sheet Resistance Assessment

A four-point probe system (Ossila, UK) was used to study the effect of the number of layers on the sheet resistance of the silver leads. This technique, also known as the Kelvin technique, is based on using four electrical probes that are equally spaced in a straight line. A current is sourced by the outer two probes, while the two inner probes measure the voltage drop. The sheet resistance of the silver films is then calculated from the resultant I-V curve according to the equation:

$$SheetResistance = \frac{\pi}{ln(2)} \frac{\Delta V}{I} \qquad (4.4)$$

A schematic of working principle of the Kelvin technique is shown in figure 4.8.
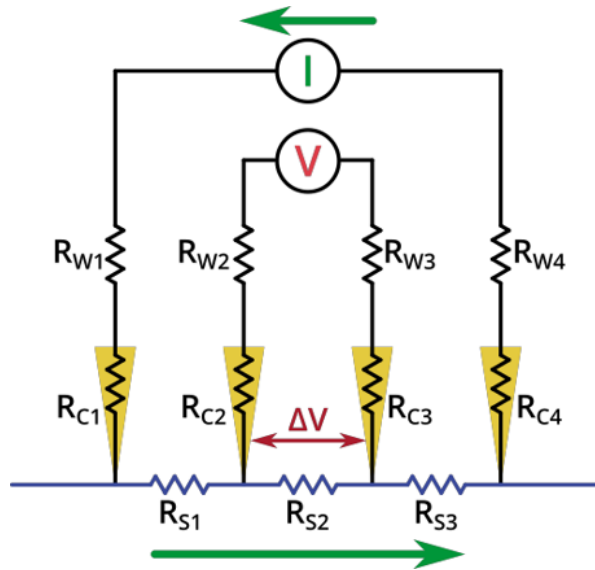
Figure 4.8: Schematic diagram of the working principle of a four-point probe circuit. Adopted from [87]

4.4.2 Device Characterization

The output and transfer characteristics of the fabricated OECTs were measured using two PXIe-4138 source measuring units operated on LabVIEW software (National Instruments). The PXIe-4138 system source-measure unit (SMU) delivers high power, precision, and speed and features 4-quadrant operation, which means it can deliver and measure any direction of current and voltage. A hardware-timed sourcing and measuring virtual instrument (VI) was used with a high-speed sequencing engine for synchronizing acquisitions between multiple SMUs. Figure 4.9a illustrates the pin-outs of used SMU. The testing pins are HI and LO, which correspond to the positive and negative terminal, respectively. The sense HI and sense LO are to account for the line resistance. The guard pins are used to remove the effects of leakage currents and parasitic capacitance between HI and LO pins. Guard terminals are driven by a unity gain buffer that follows the voltage of the HI terminal. In a typical test system where guarding is utilized, the Guard conductor is a shield surrounding the HI conductor. By making this connection, there is effectively a 0 V drop between HI and Guard, so no leakage current flows from the HI conductor to any surrounding conductors. Some leakage current might still flow from the Guard output to LO, but, since the current is being supplied by a unity gain buffer instead of HI, it does not affect the output or measurement of the SMU. The two employed SMUs were controlled using a self developed LabVIEW (National Instruments, USA) virtual Instrument (VI). The VIs for measuring the output and transfer characteristics are shown in figures B.1 and B.2 respectively. The testing of the fabricated devices is done according to the setup illustrated in figure 4.9b.

The contact resistance in the developed OECTs was characterized using the transmission-line method (TLM). In principal, The total resistance between the source and drain, denoted as the on-resistance, that is seen by the channel current can be divided into two main components; the channel resistance, which is the resistance of the OSC itself,

35

	Item	Description
A	Status Indicator	LED
B	Sense Status Indicator	LED
C	Output Connector, Terminal 0	Output LO
D	Output Connector, Terminal 1	Sense LO
E	Output Connector, Terminal 2	Guard
F	Output Connector, Terminal 3	Output HI
G	Output Connector, Terminal 4	Guard
H	Output Connector, Terminal 5	Guard
I	Output Connector, Terminal 6	Guard
J	Output Connector, Terminal 7	Sense HI
K	Binding Post	Chassis Ground

(a)

(b)

Figure 4.9: (a) Pinout of PXIe-4138. (b) Testing schematic of OECT

and the contact resistance, which is the corresponds to the contact resistance between the metal/OSC interface. A model circuit diagram of the source and drain contacts is shown in the inset of figure 5.5f. The linear region of the output curves were extracted to calculate the on-resistance of the OECT's channel using a self-developed algorithm. After that, the slopes of the linear region output $I_D - V_D$ curves were then extracted and plotted as a function of the applied gate voltage for four different channel lengths.

Aim 2: Test the ability of the developed OECT to detect picomolar concentration of BSA.

4.5 Sensitivity Assessment

To assess the sensitivity of the optimized design of the OECT, a dosing experiment was designed where increasing concentrations of BSA was sequentially fed to the sensor, while the drain current was continuously recorded. Known Increasing concentrations of BSA in PBS buffer were drop-casted onto the surface of the channel of the OECT after a stable reading using1PBS buffer was obtained. An epoxy well was designed and fabricated onto the OECT around the channel to prevent overflowing of the BSA solution out of the active site of the biosensor. The experimental setup is illustrated in 4.10. Figure 4.10a shows a top view of the active site of the sensor, and a cross section along the dashed red line is shown in figure 4.10b. The gate and drain voltage was set to the values placing the transistor in the saturation region where the transconductance is at its maximum value. Those were $V_{GS} = 0V$, and $V_D = -0.6V$. The dynamic response of the OECT biosensor The sensor was controlled using a self developed virtual instrument programmed on LabVIEW. the graphical code is shown in figure B.3.
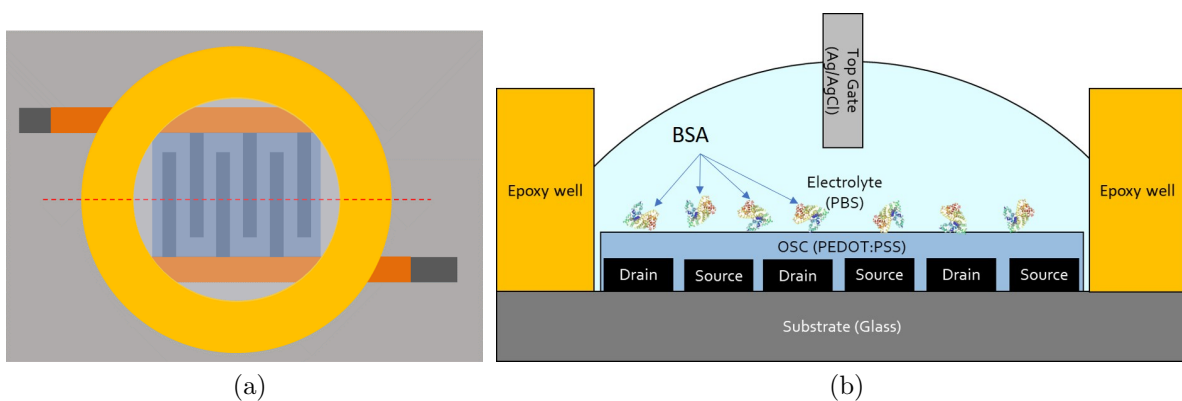
Figure 4.10: (a) schematic bird-view of the interdigitated OECT used in sensitivity assessment. (b) Testing schematic of OECT

Chapter 5

Results

In this work, different designs of OECTs were developed using inkjet-printing. the printing process was optimized for high throughput fabrication. The minimum channel length achieved was 20-25 μm using high precision digital patterning.

5.1 Sheet Resistance and PVPh uniformity

The sheet resistance of the inkjet printed patterns in the OECT, namely the source and drain, has been measured using the 4-point probe technique. As expected, the sheet resistance decreased with increasing the number of layers, and thus, the thickness of the printed films. The correlation between sheet resistance measurements and film thickness is shown in figure 5.1c. Error bars correspond to standard error ($n = 3$).

To examine the morphological changes that occur due to thermal curing of AgNPs, a scanning electron microscope (SEM) has been used. The SEM images of inkjet printed AgNPs before and after thermal curing are shown in figure 5.1a and 5.1b respectively. it is clearly demonstrated that the AgNPs fuse together to form a conductive pattern.

As for printing PVPh as a dielectric layer to insulate the leads of the source and drain, several parameters have been manipulated to overcome the film defects of the

PVPh. The main parameters manipulated are the drop spacing and the number of layers. a compilation of the results are shown in figures 5.1d, through 5.1i. The best printing quality of the PVPh ink was achieved when using drop spacing of 35 μm and printing 10 layers of PVPh. This way, we were able to achieve a uniform film thicknesses of 2.5 μm with excellent print quality.

The first iteration of the design of the silver source and drain (S&D) is shown in figure 5.2a. This design allowed the ability to easily control channel dimensions. However, in inkjet printing as explained in chapter 4, micro-topography of the surface as well as the surface chemistry greatly influence the morphology of the printed films. In this case, after printing the PVPh layer to insulate the leads, the surface chemistry of the silver nanoparticles caused the contact angle of the PVPh to be low, which pushed the PVPh to flow over the channel, therefore blocking it as shown in figure 5.2b. This issue was solved by shifting the source and drain leads up and down, respectively. This created a 90 degrees angle on the sliver, which prevented the PVPh from overflowing and blocking the channel as seen in the complete device shown in figure 5.2c. This has also allowed the fabrication of interdigitated S&D structures (figure 5.2d), which would greatly influence the performance of the OECT as described in subsequent sections.
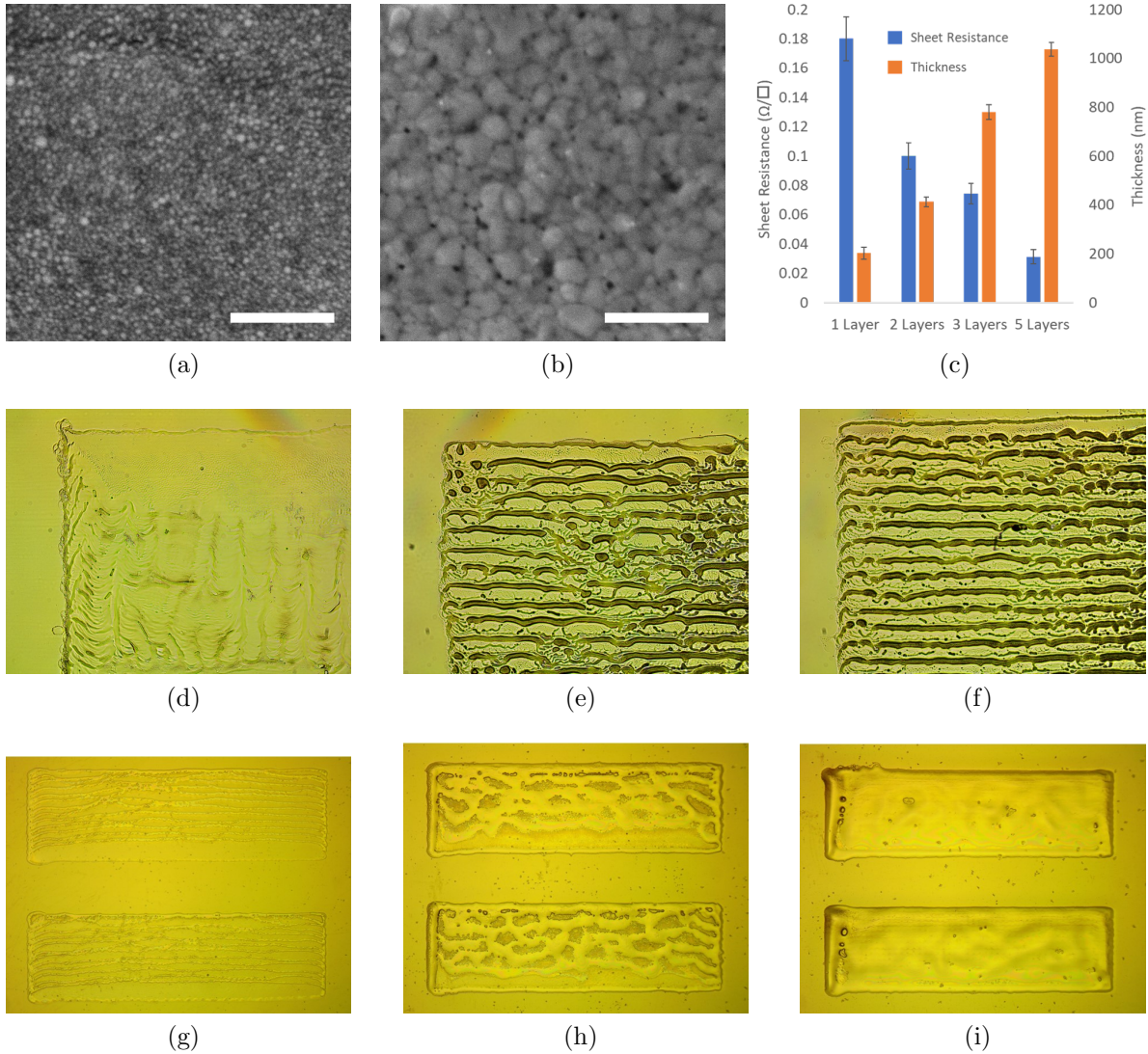
Figure 5.1: SEM images of (a) uncured AgNPs and (b) cured AgNPs after thermal curing. Scale bars indicate 500 nm. (c) Sheet resistance measurement for different layers and the corresponding printed film thickness. Error bars indicate standard error of measurements ($n = 5$). PVPh films printed with drop spacing of 15 (d,e,f) and 35 μm (g,h,i) with a number of layers of 1 (d and g), 5 (e and h), 10 (f and i).

(a)   (b)

(c)   (d)
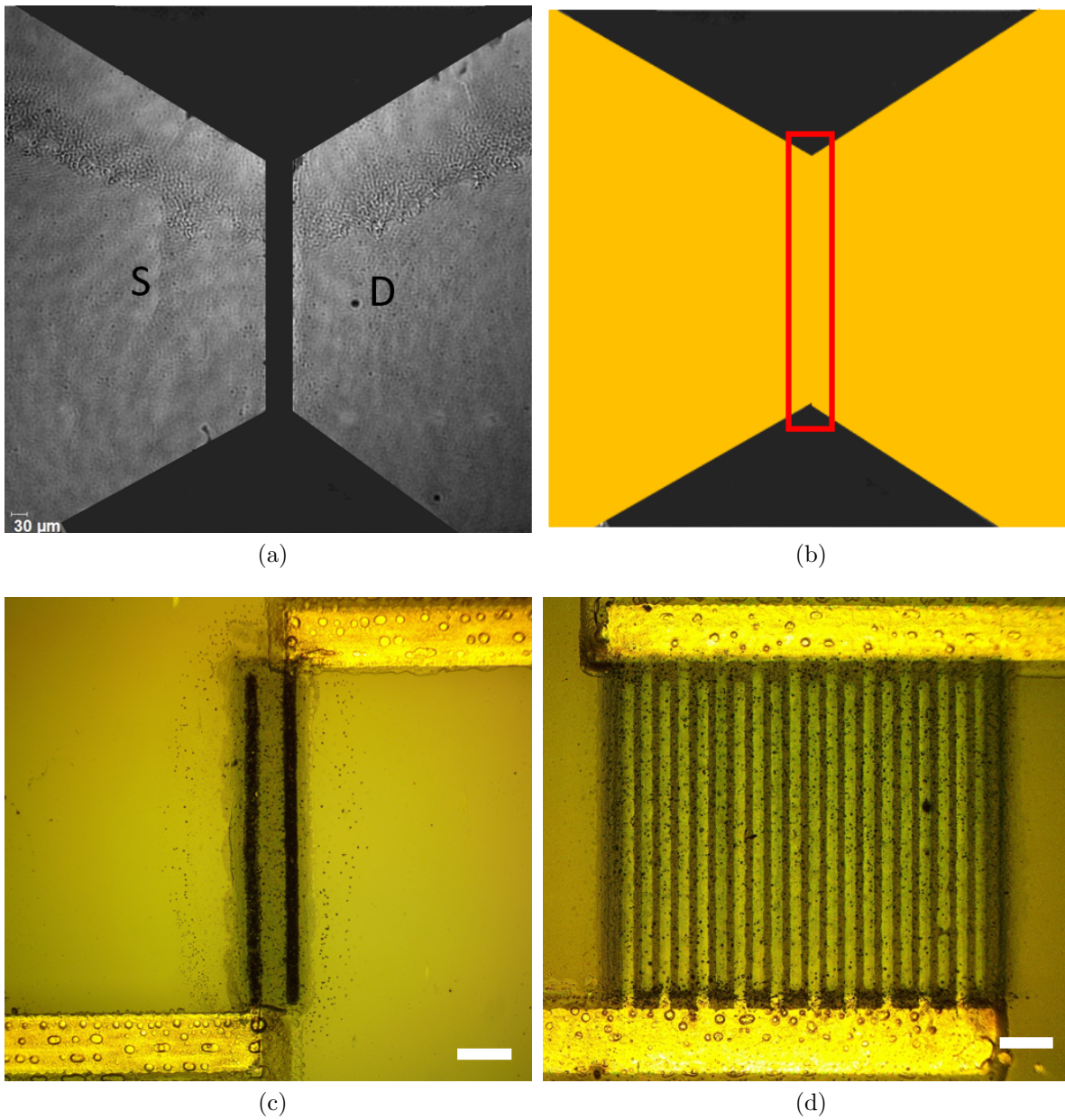
Figure 5.2: Optical micrographs of (a) silver layer of the first iteration of the design of OECTs and (b) after insulating the S&D leads with PVPh. (c) A completed device from the second iteration design of OECTs. (d) A completed device from the second iteration design of OECTs with interdigitated S&D structure. Scale bars indicate $200\mu m$.

5.2   Volumetric Capacitance

The volumetric capacitance assessment of the different PEDOT:PSS inks was conducted on 4 samples per ink. To get an accurate measure of the volumetric capacitance, 4 different channel volumes were fabricated using inkjet printing. These are as follows: 20.8, 5.2, 1.3, $and\,0.46 \times 10^{-6} cm^3$. Figure 5.3a and 5.3b shows the impedance and phase spectra, respectively for the different volumes using PEDOT:PSS-ink 2 as a sample results. The coating capacitance was extracted from each spectrum after fitting the results into the model described in chapter 4. Subsequently, each extracted coating capacitance (C_c) value was plotted as a function of the nominal volume of the PEDOT:PSS film. As is well-described by Malliaras and colleagues, there exists a linear relationship between electrochemical capacitance and OSC film volume [74, 89]. This volumetric capacitance can be estimated as the constant slope of the film capacitance with respect to its volume. It was found that the volumetric capacitance of PEDOT:PSS ink 2 at $18.524 F/cm^3$, was significantly larger than that of the other two polymer blends, both of which were less than $1 F/cm^3$.

These results served to determine the best PEDOT:PSS formulation to serve as a channel material. PEDOT:PSS ink 2 is referred to as the PEDOT:PSS-EG ink in the current and later chapters.

Figure 5.3: (a) Impedance and (b) Phase of different PEDOT:PSS-EG electrode areas. (c) Plots of extracted coating capacitance values as a function of active volume of t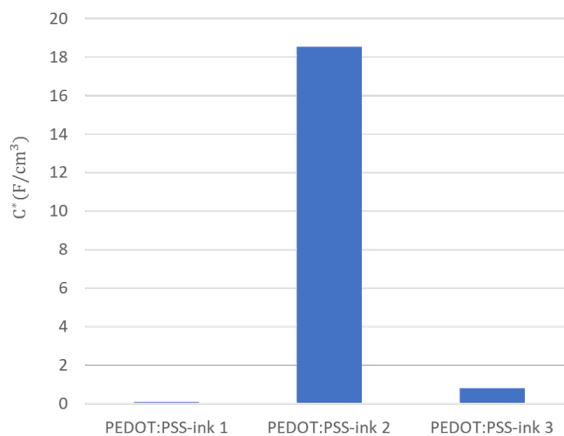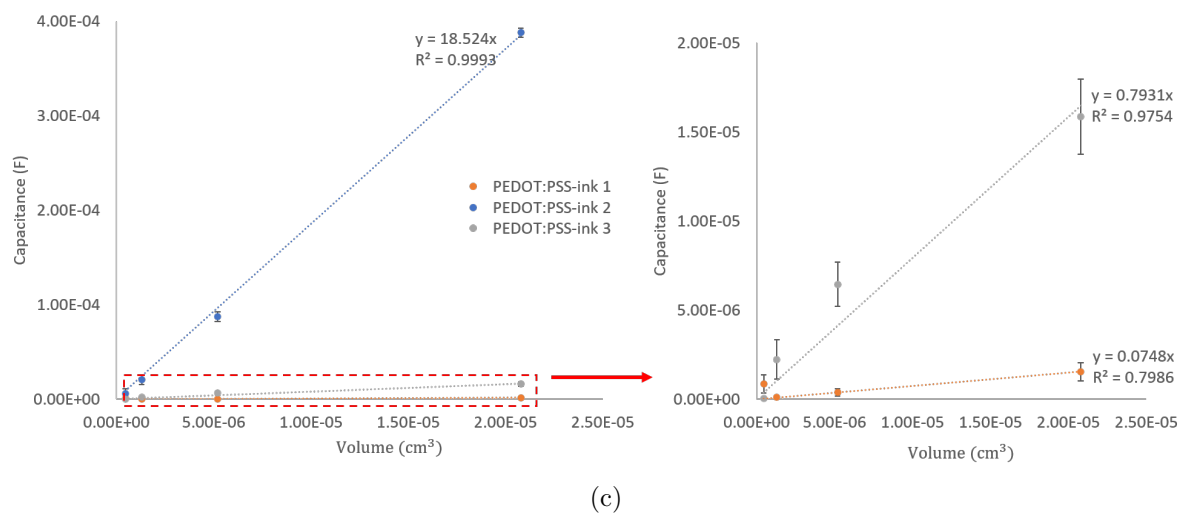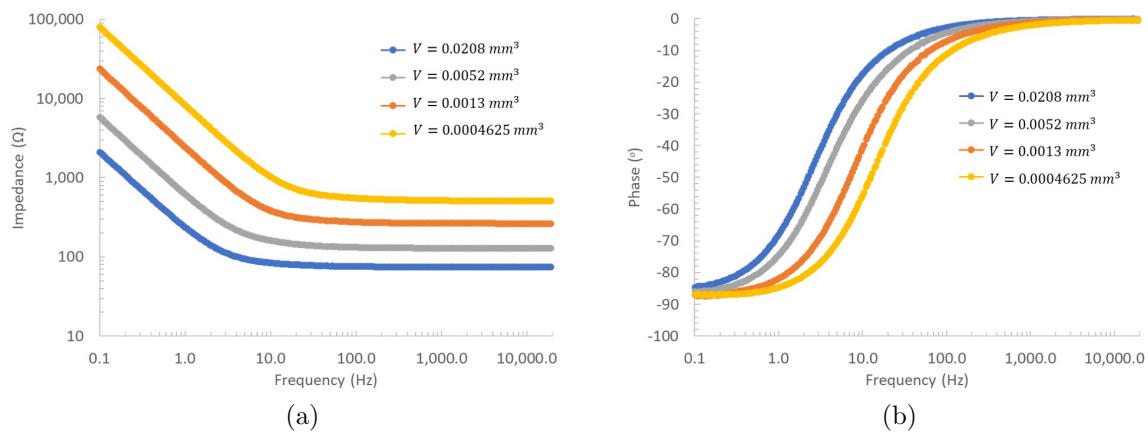he different PEDOT:PSS ink studies. Inset: coating capacitance values for inks 1 and 3. error bars indicate standard error $(n = 2)$(d) Extracted volumetric capacitance values for the studies inks.

43

5.3 Device Characteristics

After examining the 3 investigated inks and their effect on the volumetric capacitance of the PEDOT:PSS film, it was clear that the PEDOT:PSS-EG formulation produced the highest C^* value. The OECTs were then fabricated using this PEDOT:PSS formulation. Digital micrographs of the steps of fabrication are shown in figure 5.4e, 5.4f, and **??** for fabricating the interdigitated source and drain, insulating their leads, and creating the channel with the PEDOT:PSS-EG ink formulation respectively.

Figures 5.5a, 5.5b, 5.5c, and 5.5d shows the output characteristics of inkjet-printed OECTs with similar channel width and thickness and varying length. Those correspond to the devices shown in figures 5.4a,5.4b,5.4c, and 5.4d respectively. As expected, the maximum drain current level was the highest (-0.26 mA) for a gate voltage of 0 Volts for OECTs with the smallest channel length 5.5a. Since the developed OECTs exhibited very high on-state current (at $V_G = 0V$) due to the relatively high conductivity of PEDOT:PSS-EG ink, in principle, the contact resistance at a Ag/PEDOT:PSS interface can negatively affect the resultant OECT performance. The TLM analysis of the developed OECT is shown in figure 5.5e where the on-resistance is plotted with respect to the channel length. The intersection of the linear regression of the on-resistance with the y-axis represents a widely accepted estimate of to the contact resistance (R_C) that the channel current is experiencing. This R_C corresponds to sum of the drain-OSC junction resistance, as well as the OSC-source junction resistance. The width-normalized R_C was then extracted and plotted for different gate voltages as seen in figure 5.5f. A minimum value of 4.98Ω has been achieved for w-normalized R_C at $V_G = 0V$. The exponential increase in the contact resistance is signifying the profound control of the gate voltage on the channel current.
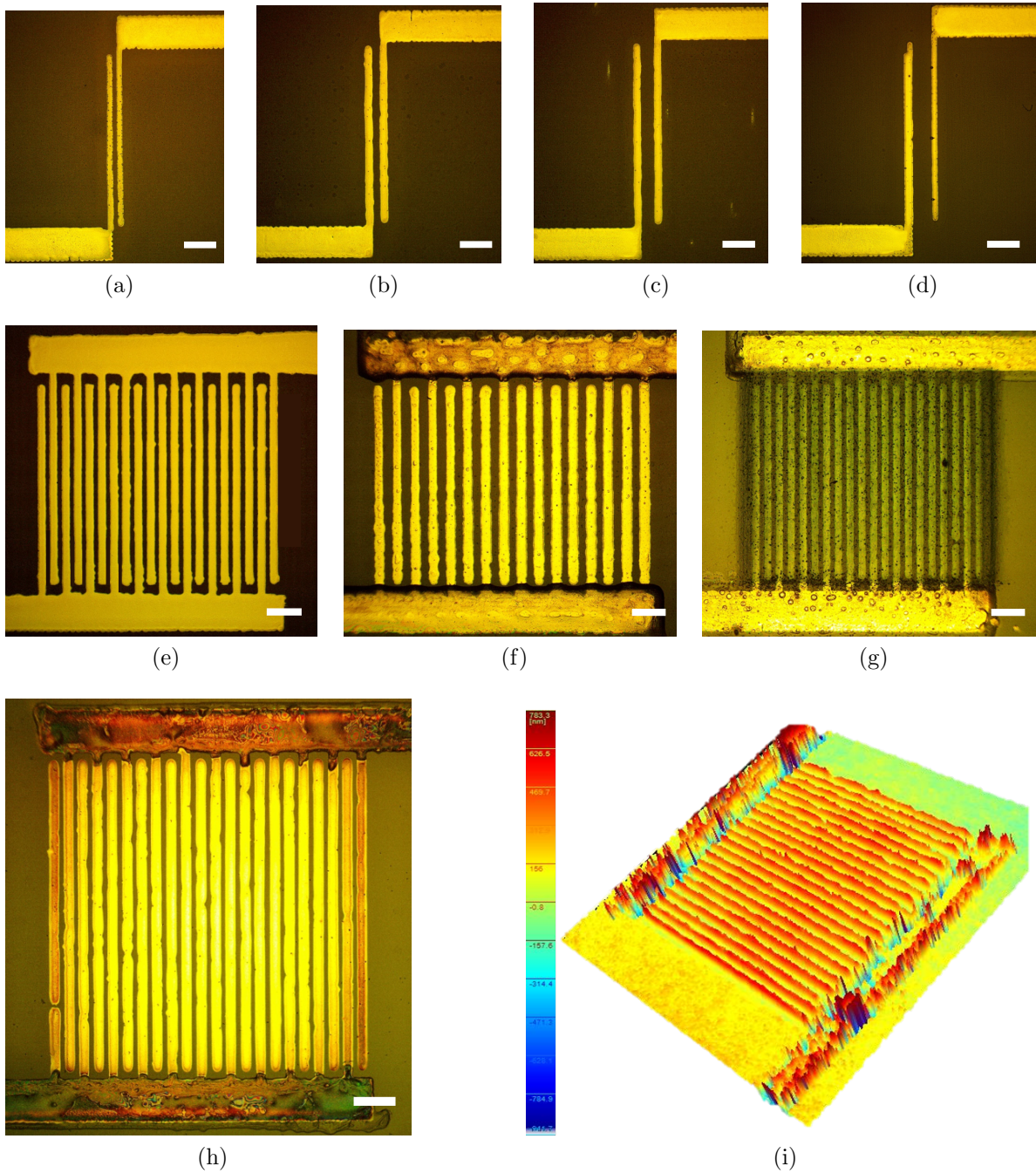
Figure 5.4: Inkjet printed OECTs with varying channel length: (a) $L = 32\mu m$, (b) $L = 56.5\mu m$,(c) $L = 94.8\mu m$ and (d)$L = 130.4\mu m$. Optical micrographs of a device with (e) interdigitated sources and drain, (f) with PVPh-insulated leads, and the final device in (g) with PEDOT:PSS channel. (h) shows the a sample device used in biosensing with a 3D-reconstructed image of the same device. Scale bars indicate $200\mu m$.

45
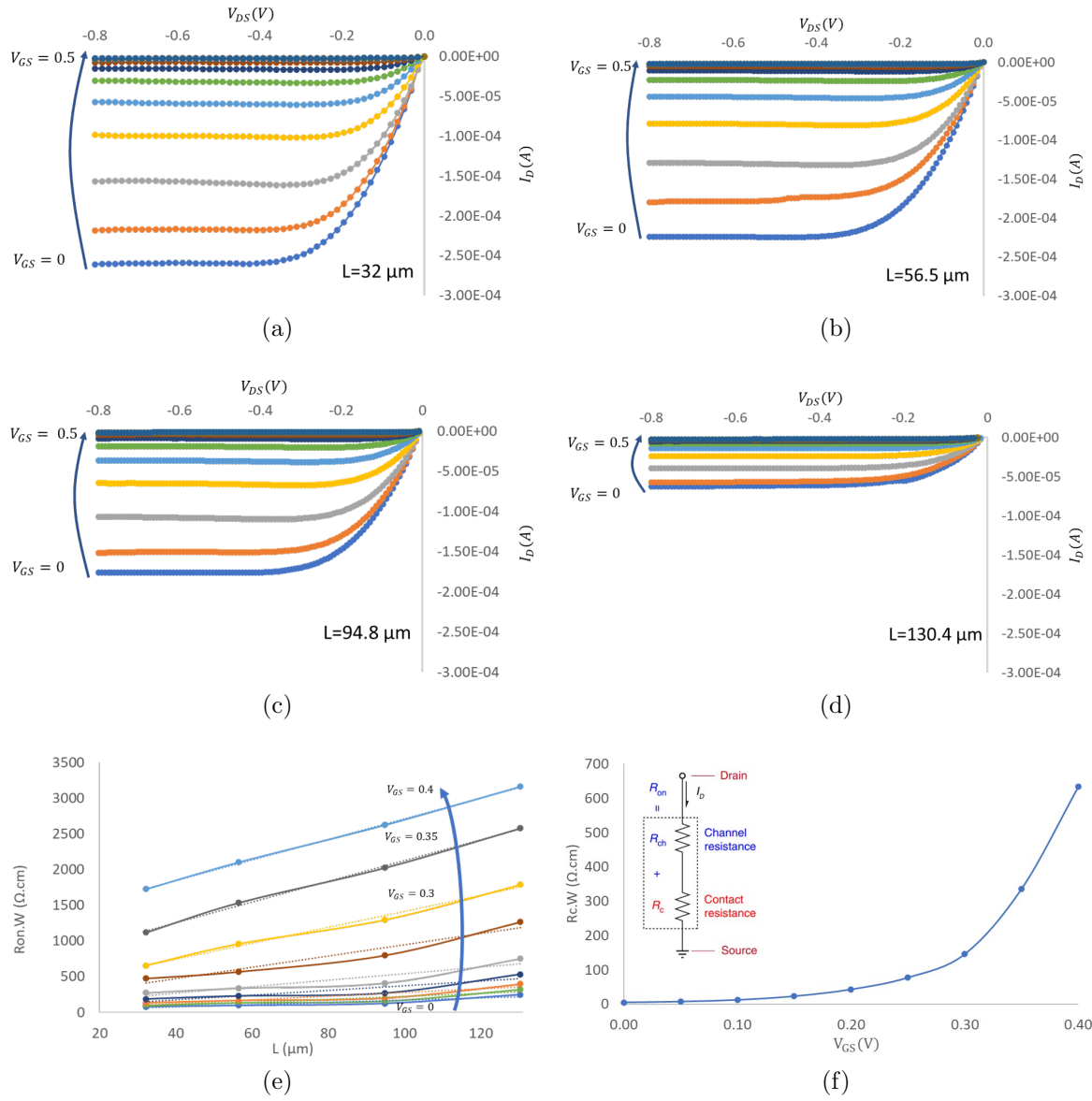
Figure 5.5: Output Characteristics of OECTs with channel lengths equal to (a) $32\,\mu$m, (b) $56.5\,\mu$m, (c) $94.8\,\mu$m, and (d) $130.4\,\mu$m. (e) Transmission line analysis of PEDOT:PSS-EG OECTs ($d = 663.44\,nm$) (f) W-normalized contact resistance as a function of the gate voltage. Inset showing the equivalent circuit model of the OECT's channel.

The transfer characteristic curves of fabricated devices with different Wd/L is shown in figure 5.6a.The drain voltage was kept at $-0.6V$ while the gate voltage was swept from $-0.2V$ to $0.6V$. For higher Wd/L ratio devices, the drain current resulted in a generally higher value as expected. It was also noticed that gate voltage corresponding to the maximum drain current shifted to more positive values for higher wd/L ratios. From the transfer characteristic curves, the transconductance curve were generated using a self-developed MATLAB code following the basic transconductance equation 2.3. The transconductance values were also verified by fitting the transfer characteristics to a polynomial function following the least square method and deriving the polynomial with respect to the gate voltage. The results are shown in figure 5.6b. The zerog_m value followed the shift in the peak I_D of the transfer curves. A compilation of the maximum transconductance values achieve from several devices with varying Wd/L is shown in figure 2.5. The figure also shows a comparison of this work with other state-of-the-art OECT designs. Rivnay et al. used gold source and drain with PEDOT:PSS as a channel material [90]. Inal et al. and Sun et al. had similar design but with PEDOT:PMATFSI and BBL as a channel material respetively. [91, 92]. Those OECTs were fabricated using photolithography coupled with spin coating the organic semiconductor followed by a lift-off process.
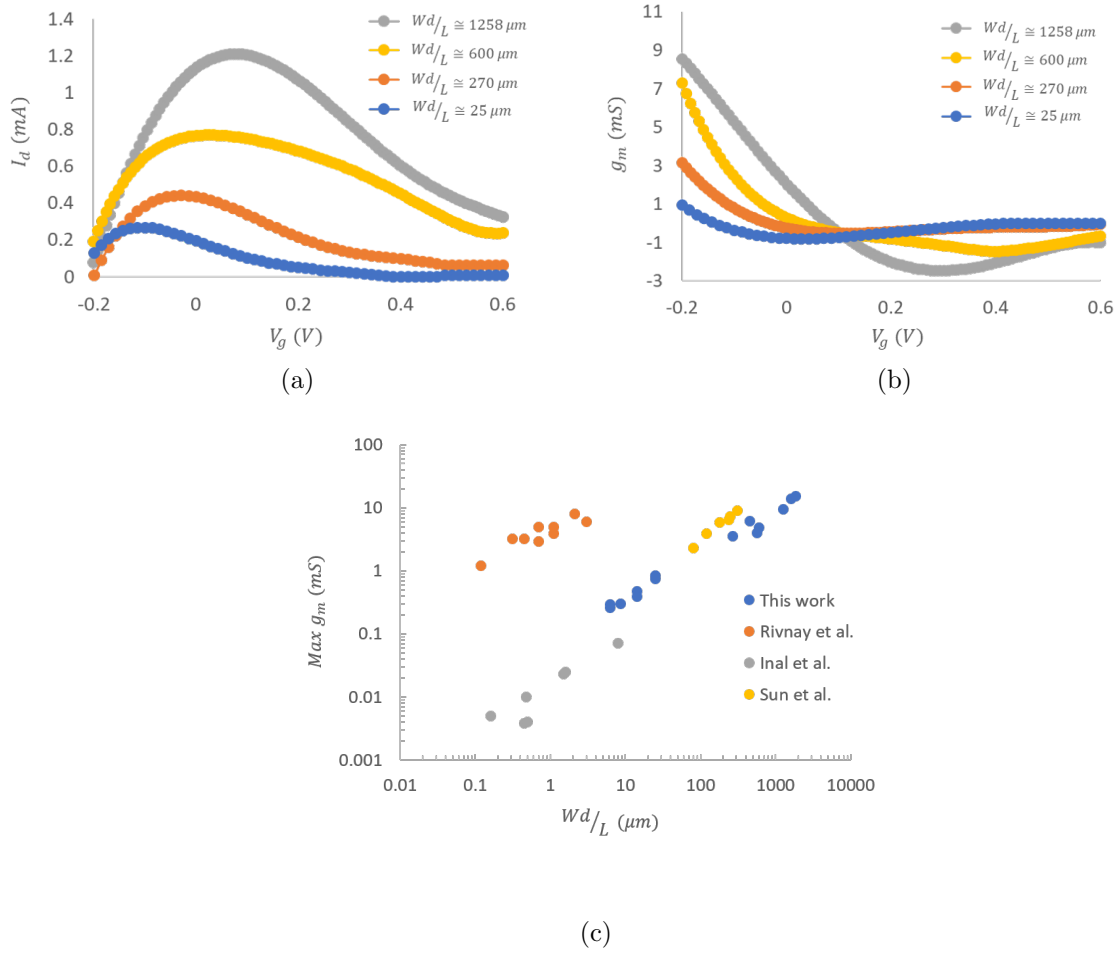
Figure 5.6: (a) Transfer characteristics of inkjet printed devices with varying Wd/L and (b) the corresponding transconductance curves. (c) Geometry scaling of peak transconductance. Data point adopted from Rivnay et al. [90], Inal et al. [91], and Sun et al. [92].

5.4 Device Sensitivity

The sensitivity of the PEDOT:PSS-EG biosensor was examined by testing it with a sequence of concentrations of BSA. The real-time dynamic response of the sensor upon injection of various concentrations of BSA at constant V_D(-0.6 V) and V_{GS}(0 V) is illustrated in figure 5.7a. The biosensor showed a relatively fast response of 20 to 30 seconds after sample loading. The drain current level of the OECT decrease in response adding different concentration of BSA into the PBS solution. A relatively constant decrease in drain current was observed for a decade increase in BSA concentration from $1pM$ to $10\mu M$. The change in drain current in response to each concentration was then plotted in figure 5.7b. The logarithmic value of BSA concentration, termed log_{BSA}, showed a linear response within the tested range. The relationship was represented the following equation:

$$\Delta I_D(\mu A) = 2.2572 \times log_{BSA} + 3.7375 \tag{5.1}$$

with a correlation coefficient of 0.9965. Error bars represent standard error of measurements ($n = 3$).
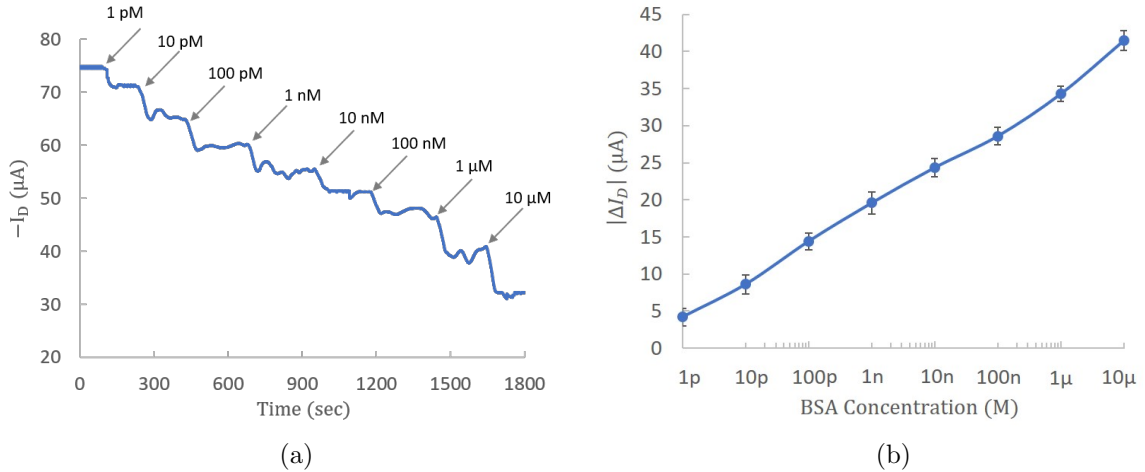
Figure 5.7: (a) Dynamic response of the optimized OECT towards BSA (b) The response of the optimized OECT to BSA at a sequence of concentrations.

Chapter 6

Discussion

In the era of distributed and tele-medicine, point of care biosensors that provide high thoughput, sensitivity, and scalability are becoming more and more the focus of development in biotechnology. Organic electrochemical transistors are being demonstrated as a powerful platform for biosensors due to their flexibility, biocompatibility, and cost-effectiveness. However, the most important factor to take into account is the unprecedented transconductance explained by the high yield in terms of ion-to-electron conversion.

Semiconductor fabrication technologies have been conventionally implemented in the fabrication of OECTs. Even though some methods, like Chemical Vapor Deposition (CVD), Physical Vapor Deposition (PVD), and photolithography offer much higher accuracy and repeatability, they are quite expensive, require a working cleanroom, and are not compatible with all the electrode and/or substrate materials. Inkjet printing technologies are emerging as suitable fabrication technologies for biosensing applications. These technologies overcome the expensive fabrication techniques of lithography and related procedures, while maintaining lower but acceptable repeatability, and accuracy . Additionally, it is compatible with a much broader range of substrates and with a much wider variety of electrode materials.

Perhaps one of the most prominent advantage of Inkjet printing is the ability to fabricate thicker films (>200 nm), which is not possible by conventional techniques. In the context of the organic semiconductor used in this work, traditional PEDOT:PSS deposition techniques of spin-coating does not permit the deposition of thick PEDOT:PSS layers. This is because such patterning usually requires a mechanical peel-off process of the PEDOT:PSS that does not succeed for thick layers, where all of the PEDOT:PSS film is be exfoliated when its thickness increases. The second method involves electrodeposition of PEDOT:PSS; this method can achieve thick layers but suffer from three main limitations: firstly, it is a serial process, meaning that electrodes are usually electrodeposited one by one which could create variabilities between electrodes. Secondly, small variations in the morphology lead to non-uniform electrochemical currents and loss of control over the resulting PEDOT:PSS films. Third, it is not possible to electrodeposite PEDOT:PSS on non conductive surfaces, where the channel of the OECT is usually created.

To realize our OECT, silver nanoparticle ink was used to pattern the source and drain electrodes. Although it is not widely adapted, the used silver nanoparticles ink showed an excellent sheet resistance with values reaching as low as $0.03\,\Omega/sq$. The non-linear decrease in the sheet resistance from layer 1 to subsequent layers, as seen in figure 5.1c, can be explained by surface defects that could happen due to imperfections in the printing process. These defects actually decrease the effective volume of the printed film, leading to an increase in sheet resistance. However, those printing defects were not observed when adding more layers, explaining the linear relation between the number of printed layers and the corresponding sheet resistance according to equation (6.1):

$$Sheet\ Resistance = \frac{\rho}{d} \tag{6.1}$$

where ρ is the material resistivity, and d is the film thickness. Another important

observation from increasing the number of layers of printed AgNPs is that the liquid ink after printing overflows outside of the bounds of the designed structure. This effect gets troublesome when printing structures that are separated by a small gap of $< 30\,\mu m$ as in the source and drain of the OECT. Increasing the number of layers of printed AgNP ink above 2 layers was shown to short the source and drain electrodes, rendering the device non-functional.

As for characterizing the organic semiconductor, PEDOT:PSS, the volumetric capacitance experiments of the three developed inks, the key findings are described as follows. First, as shown in Fig. 5.3c, the volumetric response of electrochemical capacitance is confirmed in all inks, suggesting that the adding EG and/or DMSO does not prevent ions from penetrating into the the bulk of the film. However, the orders of magnitude difference between inks 1 and 2 demonstrates that adding both EG and DMSO, leads to an antagonistic interaction that greatly affects the volumetric capacitance of the semiconductor. This result implies that a large volume density of charges could be accommodated throughout the PEDOT:PSS-EG film, which can be ascribed to the polymer conformational change described in chapter 4. Secondly, the addition of graphene to PEDOT:PSS in ink 3 did not have a significant effect on the volumetric capacitance, which could be related to the non uniform deposition of this hybrid ink onto the surface of the electrode. One possible explanation to this non-uniform deposition is the nature of the dispersion solution, which is DMF. This solvent is volatile at room temperature and pressure, which causes a significant coffee ring effect on the PEDOT:PSS/Graphene film. Additionally, we have noticed that the printed PEDOT:PSS/graphene films are not stable for a long time on aqueous medium. The printed films appeared to delaminate form the silver surface after about 5 minutes. Another reason for the low C^* value could be related to percentage of PEDOT:PSS in the ink formulation. Standing at 16.67% this might not be enough for the water and dissolved ions to penetrate deep into the

film to modulate the film's doping/dedoping mechanism.

To characterize the OSC/Ag contact, our experiments have shown that the contact resistance at the interface was as low as 4.98Ω this parameter have not been characterized for silver/PEDOT:PSS contact before. It is challenging to reach the ideal ohmic contact at a metal/organic semiconductor interface due to the ubiquitous Fermi-level pinning and deviation from the Mott-Schottky model [93, 94]. In this regard, sub-optimal charge injection and high contact resistance are considered the limiting factor to channel current in organic devices. Their effect becomes magnified in short-channel transistors [95, 96]. However, The low R_C at $V_G = 0V$ can be explained as the effect of alleviating contact depletion in the existence of a relatively large density of free charge carriers (ions) at the slightest dedoping condition. OECTs typically exhibit relatively lower R_C than solid-state OFETs by orders of magnitude, which allows OECTs to achieve significantly higher transconductance values than their OFETs counterparts.

The contact resistance measurements played a crucial role in explaining the limits of the peak transconductance reached by the inkjet printed OECTs.The fast drop of the transconductance shown in figure 5.6b can be explained by the exponential increase in contact resistance in response to increase in gate voltage. The peak geometry scaling of peak transconductance shown in figure 5.6c represent a comparison of the state-of-the-art OECTs. There exists a gap between photolithography-fabricated PEDOT:PSS OECTs with gold source and drain as reported by Rivnay et al. [90] and our inkjet printed OECTs with silver course and drain. This can be explained by the order of magnitude difference between the contact resistance between gold and PEDOT:PSS, versus that of silver. However, this shortcoming was compensated for by increasing the Wd/L ratio. That allowed us to even surpass the performance of the gold-contact OECTs in terms of transconductance.

Testing the inkjet printed biosensor on BSA showed a limit of detection as low as 1

pM. The relatively long current stability time of the OECT after adding concentrations of BSA, shown in figure 5.7a, can be explained by the change in solution conductivity, and the non specific binding of the BSA onto the surface of the channel. Although the inkjet printed biosensor was tested on BSA, it is showing potential to be applied on heart failure biomarkers (BNP and NT-proBNP). When considering the change in channel potential in response to NT-proBNP bound to the channel surface through its corresponding Ab, one can extrapolate the sensing results to get an idea on the limit of detection of NT-proBNP. This is evident by the linear response to concentrations of BSA at the range understudy (figure 5.7b), and the high change in drain current for a small change in protein concentration. The linear relationship between the BSA concentration and the change in drain current is suggesting that the principle behind the sensing mechanism is the change in the volumetric capacitance of the channel. This supported by the governing equation of the operation of OECTs (equation: 2.2) shown in chapter 2, where there is a direct relation between drain current and the C^* value. The high $\Delta I_D : Concentration$ ratio, on the other hand, is indicative of the dielectric properties of BSA. This can also be related back to NT-proBNP through examining its dielectric properties. Both of these points can be confirmed by relating the BSA layer thickness at every concentration to a change in the volumetric capacitance of the channel.

Chapter 7

Conclusion

In this Thesis, novel technologies were employed to fabricate high sensitivity organic electrochemical transistor for biosensing. Inkjet printing methodology has been optimised for printing AgNPs, PEDOT:PSS, and PVPh reliably and accurately. Optimizing this procedure required extensive knowledge in surface chemistry, material science and engineering to achieve high printing resolution and quality. The work has created a working framework of material choices, fabrication process, electrochemical, and electrical device characteristics. the work has provided key insights on materials choice, optimizing the printing process, and the testing framework with biological samples. It has also provided a proof of concept on the ability to sense biomolecules with very low limit of detection using OECTs. The novelty pursued in this work is in tailoring state-of-the-art organic devices fabricated using novel, scalable additive manufacturing process to sensing cardiac biomarkers accurately and reliably. Future work on the developed biosensor would include testing the device on heart failure biomarkers such as NT-proBNP. This would also include making the device selective to that proteins by immobilizing anti-NT-proBNP antibodies on the surface of the channel. This might include a streptavidin/biotin chemical interactions to link the protein to the channel surface. A linker silane molecule should also be utilized to immobilize the streptavidin on the sur-

face. Another approach is to use a sandwich-like structure of biotin/streptavidin/biotin to immobilize the antibodies on the surface of the channel. Additionally, gold nanoparticles ink can be used to replace the silver source and drain, which should significantly enhance the performance of the biosensor. The designed OECT brings point of care diagnostics a step closer to improve their diagnostic and prognostic value with a novel technique that allows for a variety of organic semiconductors to be printed in a wide range of thicknesses to optimized OECT performance.

Appendix A

Abbreviations

HF	Heart Failure
BNP	B-type Natriuretic Peptide
NT-proBNP	N-terminal prohormone of BNP
SPR	Surface Plasmon Resonance
DoD	Drop on Demand
CRP	C-Reactive Protein
cTn	Cardiac Troponins
TNF	Tumor Necrosis Factor
ST2	Suppression of Tumorigenicity 2
sST2	soluble Suppression of Tumorigenicity 2
LVH	Left Ventricular Hypertrophy
Ab	Antibody
TFT	Thin-Film Transistor
OTFT	Organic Thin-Film Transistor
OECT	Organic Electrochemical Transistor
PEDOT:PSS	Poly(3,4-ethylenedioxythiophene)-poly(styrenesulfonate)
C^*	Volumetric Capacitance

|	
SWCNT	Single-Wall Carbon Nanotube
TIPS Pentacene	6,13-Bis(triisopropylsilylethynyl)pentacene
ISFET	Ion-Sensitive Field-Effect Transistor
MOSFET	Metal Oxide Semiconductor Field-Effect Transistor
POC	Point-of-Care
PVPh	poly(4-vinylphenol)
EG	Ethylene Glycol
DMSO	Dimethyl sulfoxide
PMF	poly(melamine-co-formaldehyde)
DMF	Dimethylformamide
EDL	Electric Double Layer
CPE	Constant Phase Element
AgNPs	Silver Nanoparticles
PET	Poly Ethyleneterphetalate
PVP	Poly Vinyl Pyrrolidon
EIS	Electrochemical Impedance Spectroscopy
OSC	Organic Semi-Conductor
SMU	Source Measure Unit
POC	Point-of-Care
LOD	Limit of Detection
SEM	Scanning Electron Microscope
TLM	Transmission Line Measurement
CVD	Chemical Vapor Deposition
PVD	Physical Vapor Deposition
BSA	Bovine Serum Albumin
BBL	poly(benzimidazobenzophenanthroline)

Appendix B

LabVIEW Code
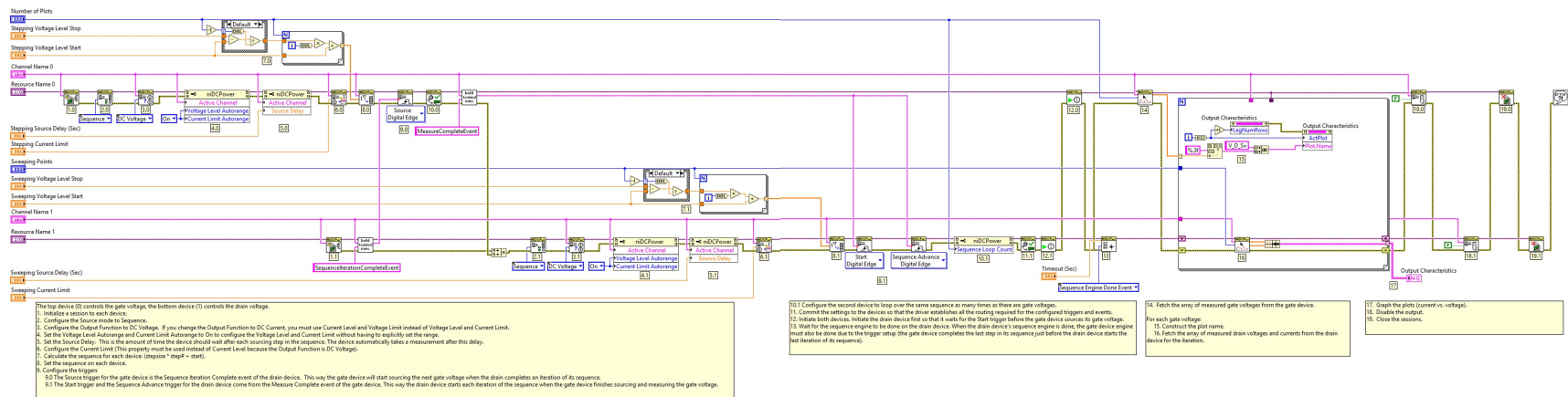
Figure B.1: Output characteristics VI
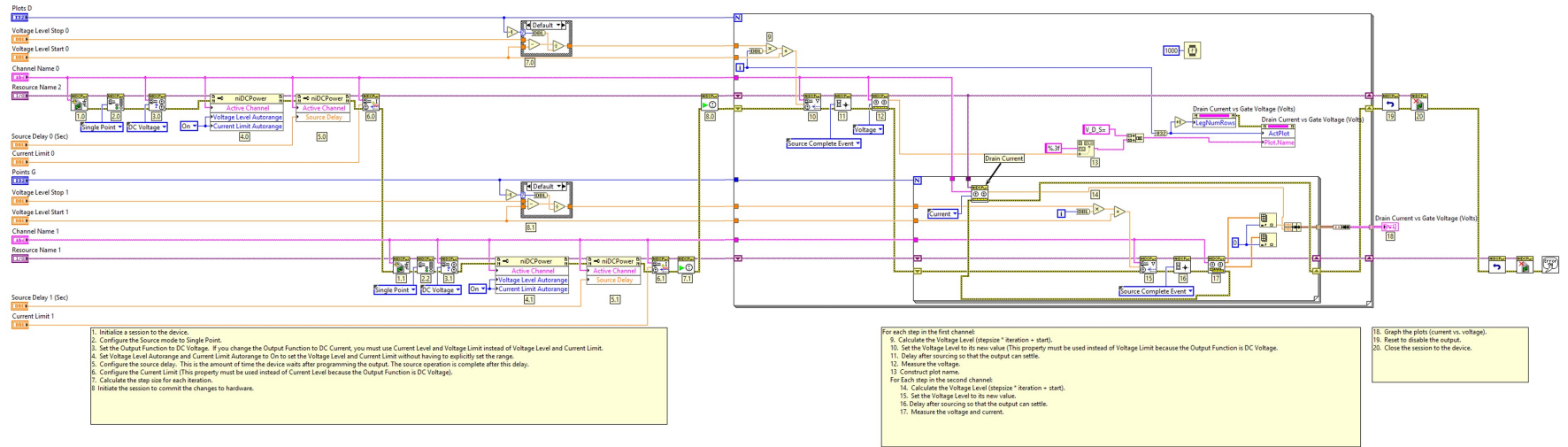
Figure B.2: Transfer characteristics VI
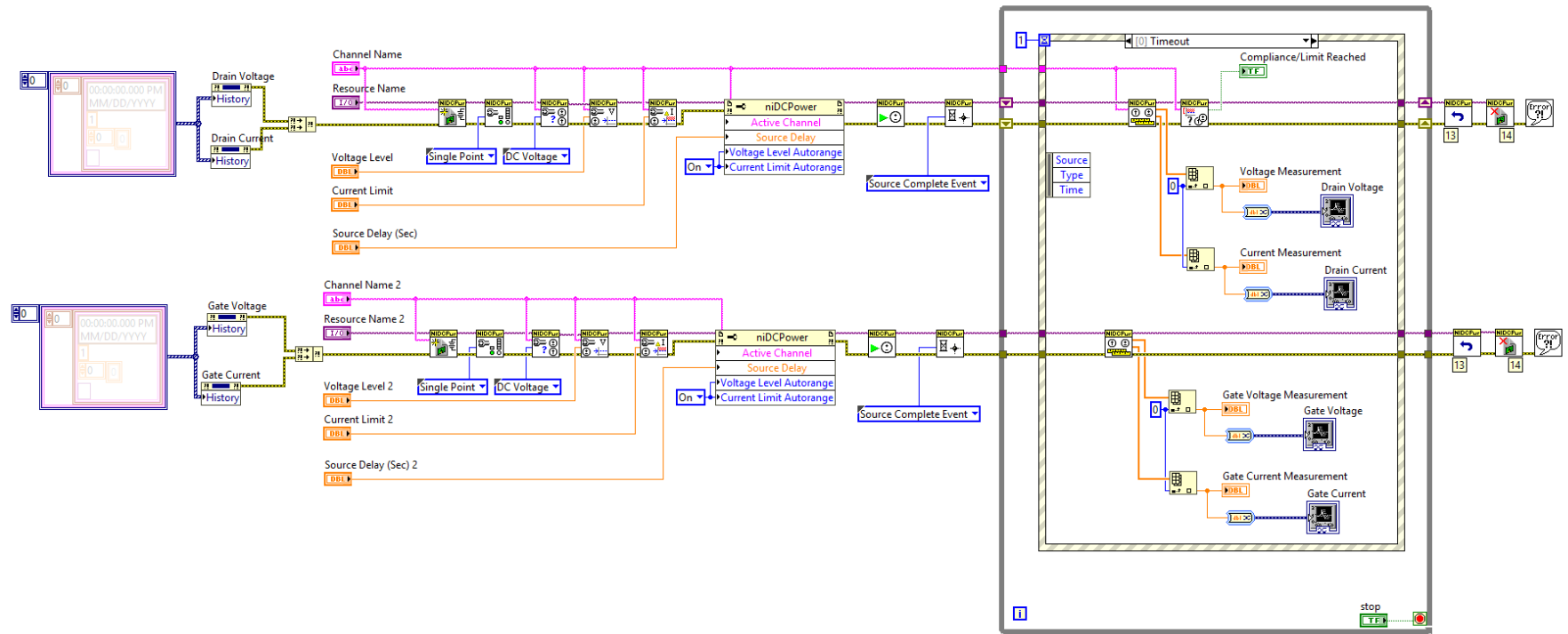
Figure B.3: Biosensing VI

Bibliography

[1] Z. Chen, G. Yang, A. Offer, M. Zhou, M. Smith, R. Peto, H. Ge, L. Yang, and G. Whitlock, "Body mass index and mortality in china: a 15-year prospective study of 220 000 men," *International journal of epidemiology*, vol. 41, no. 2, pp. 472–481, 2012.

[2] G. M. Singh, G. Danaei, F. Farzadfar, G. A. Stevens, M. Woodward, D. Wormser, S. Kaptoge, G. Whitlock, Q. Qiao, S. Lewington, *et al.*, "The age-specific quantitative effects of metabolic risk factors on cardiovascular diseases and diabetes: a pooled analysis," *PloS one*, vol. 8, no. 7, p. e65174, 2013.

[3] G. A. Mensah and D. W. Brown, "An overview of cardiovascular disease burden in the united states," *Health affairs*, vol. 26, no. 1, pp. 38–48, 2007.

[4] W. Wilson Tang, G. S. Francis, D. A. Morrow, L. K. Newby, C. P. Cannon, R. L. Jesse, A. B. Storrow, R. H. Christenson, C. MEMBERS, R. H. Christenson, *et al.*, "National academy of clinical biochemistry laboratory medicine practice guidelines: clinical utilization of cardiac biomarker testing in heart failure," *Circulation*, vol. 116, no. 5, pp. e99–e109, 2007.

[5] G. Lippi and F. Sanchis-Gomar, "Global epidemiology and future trends of heart failure,"

[6] H. Alawieh, T. El Chemaly, S. Alam, and M. Khraiche, "Towards point-of-care heart failure diagnostic platforms: Bnp and nt-probnp biosensors," *Sensors*, vol. 19, no. 22, p. 5003, 2019.

[7] D. D. Tresch, "Clinical manifestations, diagnostic assessment, and etiology of heart failure in elderly patients," *Clinics in geriatric medicine*, vol. 16, no. 3, pp. 445–456, 2000.

[8] J. A. Iwaz and A. S. Maisel, "Recent advances in point-of-care testing for natriuretic peptides: potential impact on heart failure diagnosis and management," *Expert review of molecular diagnostics*, vol. 16, no. 6, pp. 641–650, 2016.

[9] M. Mukoyama, K. Nakao, K. Hosoda, S. Suga, Y. Saito, Y. Ogawa, G. Shirakami, M. Jougasaki, K. Obata, H. Yasue, *et al.*, "Brain natriuretic peptide as a novel cardiac hormone in humans. evidence for an exquisite dual natriuretic peptide system, atrial natriuretic peptide and brain natriuretic peptide.," *The Journal of clinical investigation*, vol. 87, no. 4, pp. 1402–1412, 1991.

[10] A. Palazzuoli, M. Beltrami, M. Pellegrini, and R. Nuti, "Natriuretic peptides and ngal in heart failure: Does a link exist?," *Clinica Chimica Acta*, vol. 413, no. 23-24, pp. 1832–1838, 2012.

[11] A. Maisel, C. Mueller, K. Adams Jr, S. D. Anker, N. Aspromonte, J. G. Cleland, A. Cohen-Solal, U. Dahlstrom, A. DeMaria, S. Di Somma, *et al.*, "State of the art: using natriuretic peptide levels in clinical practice," *European journal of heart failure*, vol. 10, no. 9, pp. 824–839, 2008.

[12] H. K. Gaggin and J. L. Januzzi Jr, "Biomarkers and diagnostics in heart failure," *Biochimica et Biophysica Acta (BBA)-Molecular Basis of Disease*, vol. 1832, no. 12, pp. 2442–2450, 2013.

[13] T. Weber, J. Auer, and B. Eber, "The diagnostic and prognostic value of brain natriuretic peptide and aminoterminal (nt)-pro brain natriuretic peptide," *Current pharmaceutical design*, vol. 11, no. 4, pp. 511–525, 2005.

[14] A. Clerico, M. Fontana, L. Zyw, C. Passino, and M. Emdin, "Comparison of the diagnostic accuracy of brain natriuretic peptide (bnp) and the n-terminal part of the propeptide of bnp immunoassays in chronic and acute heart failure: a systematic review," *Clinical chemistry*, vol. 53, no. 5, pp. 813–822, 2007.

[15] R. R. van Kimmenade and J. L. Januzzi Jr, "Emerging biomarkers in heart failure," *Clinical chemistry*, vol. 58, no. 1, pp. 127–138, 2012.

[16] M. Hasanzadeh, N. Shadjou, J. Soleymani, E. Omidinia, and M. de la Guardia, "Optical immunosensing of effective cardiac biomarkers on acute myocardial infarction," *TrAC Trends in Analytical Chemistry*, vol. 51, pp. 158–168, 2013.

[17] M. E. Liquori, R. H. Christenson, P. O. Collinson, and C. R. deFilippi, "Cardiac biomarkers in heart failure," *Clinical Biochemistry*, vol. 47, no. 6, pp. 327–337, 2014.

[18] D. A. Morrow and J. A. de Lemos, "Benchmarks for the assessment of novel cardiovascular biomarkers," 2007.

[19] A. Dattagupta and S. Immaneni, "St2: Current status," *Indian heart journal*, vol. 70, pp. S96–S101, 2018.

[20] T. Mueller, I. Leitner, M. Egger, M. Haltmayer, and B. Dieplinger, "Association of the biomarkers soluble st2, galectin-3 and growth-differentiation factor-15 with heart failure and other non-cardiac diseases," *Clinica Chimica Acta*, vol. 445, pp. 155–160, 2015.

[21] M. Daamen, H.-P. Brunner-la Rocca, F. Tan, J. Hamers, and J. Schols, "Clinical diagnosis of heart failure in nursing home residents based on history, physical exam, bnp and ecg: Is it reliable?," *European Geriatric Medicine*, vol. 8, no. 1, pp. 59–65, 2017.

[22] W. W. Tang, J. P. Girod, M. J. Lee, R. C. Starling, J. B. Young, F. Van Lente, and G. S. Francis, "Plasma b-type natriuretic peptide levels in ambulatory patients with established chronic symptomatic systolic heart failure," *Circulation*, vol. 108, no. 24, pp. 2964–2966, 2003.

[23] C. W. Yancy, M. Jessup, B. Bozkurt, J. Butler, D. E. Casey, M. M. Colvin, M. H. Drazner, G. S. Filippatos, G. C. Fonarow, M. M. Givertz, *et al.*, "2017 acc/aha/hfsa focused update of the 2013 accf/aha guideline for the management of heart failure: a report of the american college of cardiology/american heart association task force on clinical practice guidelines and the heart failure society of america," *Journal of the American College of Cardiology*, vol. 70, no. 6, pp. 776–803, 2017.

[24] C. Balion, R. McKelvie, A. C. Don-Wauchope, P. L. Santaguida, M. Oremus, H. Keshavarz, S. A. Hill, R. A. Booth, U. Ali, J. A. Brown, *et al.*, "B-type natriuretic peptide-guided therapy: a systematic review," *Heart failure reviews*, vol. 19, no. 4, pp. 553–564, 2014.

[25] P. Jourdain, G. Jondeau, F. Funck, P. Gueffet, A. Le Helloco, E. Donal, J. F. Aupetit, M. C. Aumont, M. Galinier, J. C. Eicher, *et al.*, "Plasma brain natriuretic peptide-guided therapy to improve outcome in heart failure: the stars-bnp multicenter study," *Journal of the American College of Cardiology*, vol. 49, no. 16, pp. 1733–1739, 2007.

[26] A. S. Maisel, W. F. Peacock, N. McMullin, R. Jessie, G. C. Fonarow, J. Wynne, and R. M. Mills, "Timing of immunoreactive b-type natriuretic peptide levels and

treatment delay in acute decompensated heart failure: an adhere (acute decompensated heart failure national registry) analysis," *Journal of the American College of Cardiology*, vol. 52, no. 7, pp. 534–540, 2008.

[27] E. E. Egom, "Bnp and heart failure: preclinical and clinical trial data," *Journal of Cardiovascular Translational Research*, vol. 8, no. 3, pp. 149–157, 2015.

[28] R. Maalouf and S. Bailey, "A review on b-type natriuretic peptide monitoring: assays and biosensors," *Heart failure reviews*, vol. 21, no. 5, pp. 567–578, 2016.

[29] M.-I. Mohammed and M. P. Desmulliez, "Lab-on-a-chip based immunosensor principles and technologies for the detection of cardiac biomarkers: a review," *Lab on a Chip*, vol. 11, no. 4, pp. 569–595, 2011.

[30] H. Li, X. Yin, D. Sun, K. Xia, C. Kang, S. Chu, P. Zhang, H. Wang, and Y. Qiu, "Detection of nt-pro bnp using fluorescent protein modified by streptavidin as a label in immunochromatographic assay," *Sensing and Bio-Sensing Research*, vol. 11, pp. 1–7, 2016.

[31] K. D. Edwards and M. P. Tighe, "How to use n-terminal pro-brain natriuretic peptide (nt-probnp) in assessing disease severity in bronchiolitis," *Archives of Disease in Childhood-Education and Practice*, pp. edpract–2019, 2019.

[32] T. Mueller, A. Gegenhuber, W. Poelz, and M. Haltmayer, "Biochemical diagnosis of impaired left ventricular ejection fraction-comparison of the diagnostic accuracy of brain natriuretic peptide (bnp) and amino terminal probnp (nt-probnp)," *Clinical Chemistry and Laboratory Medicine (CCLM)*, vol. 42, no. 2, pp. 159–163, 2004.

[33] Z. Altintas, W. M. Fakanya, and I. E. Tothill, "Cardiovascular disease detection using bio-sensing techniques," *Talanta*, vol. 128, pp. 177–186, 2014.

[34] Y.-M. Lei, M.-M. Xiao, Y.-T. Li, L. Xu, H. Zhang, Z.-Y. Zhang, and G.-J. Zhang, "Detection of heart failure-related biomarker in whole blood with graphene field effect transistor biosensor," *Biosensors and Bioelectronics*, vol. 91, pp. 1–7, 2017.

[35] L. Basiricò, P. Cosseddu, B. Fraboni, and A. Bonfiglio, "Inkjet printing of transparent, flexible, organic transistors," *Thin Solid Films*, vol. 520, no. 4, pp. 1291–1294, 2011.

[36] P. M. Grubb, H. Subbaraman, S. Park, D. Akinwande, and R. T. Chen, "Inkjet printing of high performance transistors with micron order chemically set gaps," *Scientific reports*, vol. 7, no. 1, pp. 1–8, 2017.

[37] B. Thakur, G. Zhou, J. Chang, H. Pu, B. Jin, X. Sui, X. Yuan, C.-H. Yang, M. Magruder, and J. Chen, "Rapid detection of single e. coli bacteria using a graphene-based field-effect transistor device," *Biosensors and Bioelectronics*, vol. 110, pp. 16–22, 2018.

[38] Y. Huang, X. Dong, Y. Liu, L.-J. Li, and P. Chen, "Graphene-based biosensors for detection of bacteria and their metabolic activities," *Journal of Materials Chemistry*, vol. 21, no. 33, pp. 12358–12362, 2011.

[39] S. Afsahi, M. B. Lerner, J. M. Goldstein, J. Lee, X. Tang, D. A. Bagarozzi Jr, D. Pan, L. Locascio, A. Walker, F. Barron, *et al.*, "Novel graphene-based biosensor for early detection of zika virus infection," *Biosensors and Bioelectronics*, vol. 100, pp. 85–88, 2018.

[40] Y. Liang, M. Ernst, F. Brings, D. Kireev, V. Maybeck, A. Offenhäusser, and D. Mayer, "High performance flexible organic electrochemical transistors for monitoring cardiac action potential," *Advanced healthcare materials*, vol. 7, no. 19, p. 1800304, 2018.

[41] E. Bihar, Y. Deng, T. Miyake, M. Saadaoui, G. G. Malliaras, and M. Rolandi, "A disposable paper breathalyzer with an alcohol sensing organic electrochemical transistor," *Scientific reports*, vol. 6, p. 27582, 2016.

[42] Z.-T. Zhu, J. T. Mabeck, C. Zhu, N. C. Cady, C. A. Batt, and G. G. Malliaras, "A simple poly (3, 4-ethylene dioxythiophene)/poly (styrene sulfonic acid) transistor for glucose sensing at neutral ph," *Chemical communications*, no. 13, pp. 1556–1557, 2004.

[43] H. Tang, P. Lin, H. L. Chan, and F. Yan, "Highly sensitive dopamine biosensors based on organic electrochemical transistors," *Biosensors and Bioelectronics*, vol. 26, no. 11, pp. 4559–4563, 2011.

[44] C. H. Mak, C. Liao, Y. Fu, M. Zhang, C. Y. Tang, Y. H. Tsang, H. L. Chan, and F. Yan, "Highly-sensitive epinephrine sensors based on organic electrochemical transistors with carbon nanomaterial modified gate electrodes," *Journal of materials chemistry C*, vol. 3, no. 25, pp. 6532–6538, 2015.

[45] A. Romeo, G. Tarabella, P. DAngelo, C. Caffarra, D. Cretella, R. Alfieri, P. G. Petronini, and S. Iannotta, "Drug-induced cellular death dynamics monitored by a highly sensitive organic electrochemical system," *Biosensors and Bioelectronics*, vol. 68, pp. 791–797, 2015.

[46] P. Lin, X. Luo, I.-M. Hsing, and F. Yan, "Organic electrochemical transistors integrated in flexible microfluidic systems and used for label-free dna sensing," *Advanced Materials*, vol. 23, no. 35, pp. 4035–4040, 2011.

[47] W. Tao, P. Lin, J. Hu, S. Ke, J. Song, and X. Zeng, "A sensitive dna sensor based on an organic electrochemical transistor using a peptide nucleic acid-modified

nanoporous gold gate electrode," *RSC advances*, vol. 7, no. 82, pp. 52118–52124, 2017.

[48] D.-J. Kim, N.-E. Lee, J.-S. Park, I.-J. Park, J.-G. Kim, and H. J. Cho, "Organic electrochemical transistor based immunosensor for prostate specific antigen (psa) detection using gold nanoparticles for signal amplification," *Biosensors and Bioelectronics*, vol. 25, no. 11, pp. 2477–2482, 2010.

[49] V. Serafín, R. Torrente-Rodríguez, A. González-Cortés, P. G. De Frutos, M. Sabaté, S. Campuzano, P. Yáñez-Sedeño, and J. M. Pingarrón, "An electrochemical immunosensor for brain natriuretic peptide prepared with screen-printed carbon electrodes nanostructured with gold nanoparticles grafted through aryl diazonium salt chemistry," *Talanta*, vol. 179, pp. 131–138, 2018.

[50] A. P. Selvam, K. M. Vattipalli, and S. Prasad, "Design of a high sensitive non-faradaic impedimetric sensor," in *2012 Annual International Conference of the IEEE Engineering in Medicine and Biology Society*, pp. 3251–3254, IEEE, 2012.

[51] S. K. Moore, "Just one word-plastics," *Ieee Spectrum*, vol. 39, no. 9, pp. 55–59, 2002.

[52] H. Klauk, M. Halik, U. Zschieschang, F. Eder, G. Schmid, and C. Dehm, "Pentacene organic transistors and ring oscillators on glass and on flexible polymeric substrates," *Applied Physics Letters*, vol. 82, no. 23, pp. 4175–4177, 2003.

[53] J. B. Lee and V. Subramanian, "Organic transistors on fiber: a first step towards electronic textiles," in *IEEE International Electron Devices Meeting 2003*, pp. 8–3, IEEE, 2003.

[54] H. Klauk, M. Halik, U. Zschieschang, G. Schmid, W. Radlik, and W. Weber, "High-mobility polymer gate dielectric pentacene thin film transistors," *Journal of Applied Physics*, vol. 92, no. 9, pp. 5259–5263, 2002.

[55] M. Mizukami, N. Hirohata, T. Iseki, K. Ohtawara, T. Tada, S. Yagyu, T. Abe, T. Suzuki, Y. Fujisaki, Y. Inoue, *et al.*, "Flexible am oled panel driven by bottom-contact otfts," *IEEE electron device letters*, vol. 27, no. 4, pp. 249–251, 2006.

[56] E. Cantatore, T. C. Geuns, G. H. Gelinck, E. van Veenendaal, A. F. Gruijthuijsen, L. Schrijnemakers, S. Drews, and D. M. De Leeuw, "A 13.56-mhz rfid system based on organic transponders," *IEEE Journal of solid-state circuits*, vol. 42, no. 1, pp. 84–92, 2006.

[57] D. Briand, A. Oprea, J. Courbat, and N. Bârsan, "Making environmental sensors on plastic foil," *Materials Today*, vol. 14, no. 9, pp. 416–423, 2011.

[58] M. Takamiya, T. Sekitani, Y. Kato, H. Kawaguchi, T. Someya, and T. Sakurai, "An organic fet sram with back gate to increase static noise margin and its application to braille sheet display," *IEEE Journal of Solid-State Circuits*, vol. 42, no. 1, pp. 93–100, 2006.

[59] M. Guerin, A. Daami, S. Jacob, E. Bergeret, E. Bènevent, P. Pannier, and R. Coppard, "High-gain fully printed organic complementary circuits on flexible plastic foils," *IEEE transactions on electron devices*, vol. 58, no. 10, pp. 3587–3593, 2011.

[60] B. Kumar, B. K. Kaushik, and Y. S. Negi, "Organic thin film transistors: structures, models, materials, fabrication, and applications: a review," *Polymer Reviews*, vol. 54, no. 1, pp. 33–111, 2014.

[61] J. Rivnay, S. Inal, A. Salleo, R. M. Owens, M. Berggren, and G. G. Malliaras, "Organic electrochemical transistors," *Nature Reviews Materials*, vol. 3, no. 2, pp. 1–14, 2018.

[62] N. Coppedè, G. Tarabella, M. Villani, D. Calestani, S. Iannotta, and A. Zappettini, "Human stress monitoring through an organic cotton-fiber biosensor," *Journal of Materials Chemistry B*, vol. 2, no. 34, pp. 5620–5626, 2014.

[63] C. Liao, C. Mak, M. Zhang, H. L. Chan, and F. Yan, "Flexible organic electrochemical transistors for highly selective enzyme biosensors and used for saliva testing," *Advanced materials*, vol. 27, no. 4, pp. 676–681, 2015.

[64] R.-X. He, M. Zhang, F. Tan, P. H. Leung, X.-Z. Zhao, H. L. Chan, M. Yang, and F. Yan, "Detection of bacteria with organic electrochemical transistors," *Journal of Materials Chemistry*, vol. 22, no. 41, pp. 22072–22076, 2012.

[65] P. Lin, F. Yan, J. Yu, H. L. Chan, and M. Yang, "The application of organic electrochemical transistors in cell-based biosensors," *Advanced Materials*, vol. 22, no. 33, pp. 3655–3660, 2010.

[66] J. Rivnay, M. Ramuz, P. Leleux, A. Hama, M. Huerta, and R. M. Owens, "Organic electrochemical transistors for cell-based impedance sensing," *Applied Physics Letters*, vol. 106, no. 4, p. 8_1, 2015.

[67] A. Campana, T. Cramer, D. T. Simon, M. Berggren, and F. Biscarini, "Electrocardiographic recording with conformable organic electrochemical transistor fabricated on resorbable bioscaffold," *Advanced Materials*, vol. 26, no. 23, pp. 3874–3878, 2014.

[68] D. Khodagholy, T. Doublet, P. Quilichini, M. Gurfinkel, P. Leleux, A. Ghestem, E. Ismailova, T. Hervé, S. Sanaur, C. Bernard, *et al.*, "In vivo recordings of brain

activity using organic transistors," *Nature communications*, vol. 4, no. 1, pp. 1–7, 2013.

[69] L. Kergoat, B. Piro, M. Berggren, G. Horowitz, and M.-C. Pham, "Advances in organic transistor-based biosensors: from organic electrochemical transistors to electrolyte-gated organic field-effect transistors," *Analytical and bioanalytical chemistry*, vol. 402, no. 5, pp. 1813–1826, 2012.

[70] D. Khodagholy, J. Rivnay, M. Sessolo, M. Gurfinkel, P. Leleux, L. H. Jimison, E. Stavrinidou, T. Herve, S. Sanaur, R. M. Owens, *et al.*, "High transconductance organic electrochemical transistors," *Nature communications*, vol. 4, no. 1, pp. 1–6, 2013.

[71] L. Basiricò, "Inkjet printing of organic transistor devices," *University of Cagliari*, 2012.

[72] A. Susloparova, *Impedimetric detection of anticancer drug action on individual tumor cells using field-effect transistor devices.* Verlag nicht ermittelbar, 2016.

[73] M. Nikolou and G. G. Malliaras, "Applications of poly (3, 4-ethylenedioxythiophene) doped with poly (styrene sulfonic acid) transistors in chemical and biological sensors," *The Chemical Record*, vol. 8, no. 1, pp. 13–22, 2008.

[74] J. Rivnay, P. Leleux, M. Ferro, M. Sessolo, A. Williamson, D. A. Koutsouras, D. Khodagholy, M. Ramuz, X. Strakosas, R. M. Owens, *et al.*, "High-performance transistors for bioelectronics through tuning of channel thickness," *Science advances*, vol. 1, no. 4, p. e1400251, 2015.

[75] J. T. Friedlein, R. R. McLeod, and J. Rivnay, "Device physics of organic electrochemical transistors," *Organic Electronics*, vol. 63, pp. 398–414, 2018.

[76] C.-L. Fan, M.-C. Shang, B.-J. Li, Y.-Z. Lin, S.-J. Wang, and W.-D. Lee, "A self-aligned a-igzo thin-film transistor using a new two-photo-mask process with a continuous etching scheme," *Materials*, vol. 7, no. 8, pp. 5761–5768, 2014.

[77] O. A. Basaran, "Small-scale free surface flows with breakup: Drop formation and emerging applications," *American Institute of Chemical Engineers. AIChE Journal*, vol. 48, no. 9, p. 1842, 2002.

[78] Y. He, R. D. Wildman, C. J. Tuck, S. D. Christie, and S. Edmondson, "An investigation of the behavior of solvent based polycaprolactone ink for material jetting," *Scientific reports*, vol. 6, p. 20852, 2016.

[79] C. Ainsley, N. Reis, and B. Derby, "Freeform fabrication by controlled droplet deposition of powder filled melts," *Journal of materials science*, vol. 37, no. 15, pp. 3155–3161, 2002.

[80] B. Derby, "Inkjet printing of functional and structural materials: fluid property requirements, feature stability, and resolution," *Annual Review of Materials Research*, vol. 40, pp. 395–414, 2010.

[81] H. Dong, W. W. Carr, and J. F. Morris, "An experimental study of drop-on-demand drop formation," *Physics of fluids*, vol. 18, no. 7, p. 072102, 2006.

[82] H. Dong, W. W. Carr, and J. F. Morris, "Visualization of drop-on-demand inkjet: Drop formation and deposition," *Review of Scientific Instruments*, vol. 77, no. 8, p. 085101, 2006.

[83] E. Garnett and D. Ginley, "Electrical and morphological properties of inkjet printed pedot/pss films," *Journal of Undergraduate Research*, vol. 5, 2005.

[84] J. Ouyang, Q. Xu, C.-W. Chu, Y. Yang, G. Li, and J. Shinar, "On the mechanism of conductivity enhancement in poly (3, 4-ethylenedioxythiophene): poly (styrene

sulfonate) film through solvent treatment," *Polymer*, vol. 45, no. 25, pp. 8443–8450, 2004.

[85] S. R. Cho, Y. Porte, Y. C. Kim, and J.-M. Myoung, "Effect of nonionic surfactant additive in pedot: Pss on pfo emission layer in organic–inorganic hybrid light-emitting diode," *ACS applied materials & interfaces*, vol. 10, no. 11, pp. 9612–9619, 2018.

[86] B. K. Tehrani, C. Mariotti, B. S. Cook, L. Roselli, and M. M. Tentzeris, "Development, characterization, and processing of thin and thick inkjet-printed dielectric films," *Organic Electronics*, vol. 29, pp. 135–141, 2016.

[87] M. Grouchko, A. Kamyshny, C. F. Mihailescu, D. F. Anghel, and S. Magdassi, "Conductive inks with a built-in mechanism that enables sintering at room temperature," *ACS nano*, vol. 5, no. 4, pp. 3354–3359, 2011.

[88] M. Ryu, J. H. Yang, Y. Ahn, M. Sim, K. H. Lee, K. Kim, T. Lee, S.-J. Yoo, S. Y. Kim, C. Moon, *et al.*, "Enhancement of interface characteristics of neural probe based on graphene, zno nanowires, and conducting polymer pedot," *ACS Applied Materials & Interfaces*, vol. 9, no. 12, pp. 10577–10586, 2017.

[89] C. M. Proctor, J. Rivnay, and G. G. Malliaras, "Understanding volumetric capacitance in conducting polymers," *Journal of Polymer Science Part B: Polymer Physics*, vol. 54, no. 15, pp. 1433–1436, 2016.

[90] J. Rivnay, S. Inal, B. A. Collins, M. Sessolo, E. Stavrinidou, X. Strakosas, C. Tassone, D. M. Delongchamp, and G. G. Malliaras, "Structural control of mixed ionic and electronic transport in conducting polymers," *Nature communications*, vol. 7, no. 1, pp. 1–9, 2016.

[91] S. Inal, J. Rivnay, A. I. Hofmann, I. Uguz, M. Mumtaz, D. Katsigiannopoulos, C. Brochon, E. Cloutet, G. Hadziioannou, and G. G. Malliaras, "Organic electrochemical transistors based on pedot with different anionic polyelectrolyte dopants," *Journal of Polymer Science Part B: Polymer Physics*, vol. 54, no. 2, pp. 147–151, 2016.

[92] H. Sun, M. Vagin, S. Wang, X. Crispin, R. Forchheimer, M. Berggren, and S. Fabiano, "Complementary logic circuits based on high-performance n-type organic electrochemical transistors," *Advanced Materials*, vol. 30, no. 9, p. 1704916, 2018.

[93] A. Kahn, N. Koch, and W. Gao, "Electronic structure and electrical properties of interfaces between metals and π-conjugated molecular films," *Journal of Polymer Science Part B: Polymer Physics*, vol. 41, no. 21, pp. 2529–2548, 2003.

[94] M. Oehzelt, N. Koch, and G. Heimel, "Organic semiconductor density of states controls the energy level alignment at electrode interfaces," *Nature communications*, vol. 5, no. 1, pp. 1–8, 2014.

[95] C. H. Kim, Y. Bonnassieux, and G. Horowitz, "Charge distribution and contact resistance model for coplanar organic field-effect transistors," *IEEE transactions on electron devices*, vol. 60, no. 1, pp. 280–287, 2012.

[96] D. Natali and M. Caironi, "Charge injection in solution-processed organic field-effect transistors: Physics, models and characterization methods," *Advanced Materials*, vol. 24, no. 11, pp. 1357–1387, 2012.